Instrumented electromagnetic generator: optimized performance by automatic self-adaptation of the generator structure

Pedro M. R. Carneiro[1,2,*], João V. Vidal[3,4,*], Pedro Rolo[1], Inês Peres[1], Jorge A.F. Ferreira[1,2], Andrei L. Kholkin[3,5], Marco P. Soares dos Santos[1,2,*]

[1] Department of Mechanical Engineering, University of Aveiro, 3810-193 Aveiro, Portugal.

[2] Centre for Mechanical Technology & Automation (TEMA), University of Aveiro, 3810-193 Aveiro, Portugal

[3] Department of Physics and CICECO – Aveiro Institute of Materials, University of Aveiro, 3810-193 Aveiro, Portugal

[4] Department of Physics and I3N, University of Aveiro, 3810-193 Aveiro, Portugal

[5] Laboratory of Functional Low-Dimensional Structures, National University of Science and Technology MISIS, Moscow, Russia

* Corresponding authors: Pedro Carneiro (pedro.carneiro@ua.pt), João V. Vidal (jvsv@ua.pt), Marco P. Soares dos Santos (marco.santos@ua.pt)

Abstract

Electromagnetic generators are widely used to power both small-scale and large-scale devices. They are suitable to operate as self-powering technologies, allowing customizable upscaling and downscaling, ensuring low production and maintenance costs, and even able to integrate into hybrid solutions. As their architectures are well-suited to power a broad range of multifunctional devices, their performance optimization is a research topic of utmost importance. Their performance, strongly dependent on the frequency and amplitude of mechanical excitations and hysteretic behaviors, still needs to be improved. In this paper, a theoretical and experimental study is provided to demonstrate the effectiveness of a new concept of self-adaptive electromagnetic generator. An instrumented generator using a magnetic levitation architecture was implemented using a stepper motor, an accelerometer and a processing system. Self-adaptability was realized by changing the generator's effective length and resonance frequency as a function of the mechanical excitation characteristics. Considering the power consumption of instrumentation, output power gains around 30% were achieved under conditions of harmonic inputs with time changing frequencies and amplitudes. These are very promising results that highlight the potential of self-adaptive energy harvesting technologies for opening new research directions towards the emerging of a new line of highly sophisticated autonomous generators.

Keywords

Energy generation, self-powering, electromagnetic generator, magnetic levitation, adaptive generator, resonance tuning

1. Introduction

The development of high-performance energy harvesting technologies is a worldwide cutting-edge research topic for both small-scale and large-scale powering [1-3]. Remote sensors and/or actuators [4], mobile devices [5], portable and wearable systems [6], and intracorporeal biomedical devices [7, 8] are some examples of using self-powering technologies for ever-increasing small-scale harvesters. Battery-free solutions have been proposed for the cases when high energy demanding stand-alone operations are not needed, which is increasingly common due to the multifunctionality of a large number of actuators, sensors, communication and processing systems [9, 10]. Besides, their replacement must be significantly minimized, mainly in bioelectronic intracorporeal medical devices, not only to avoid unnecessary risks related to surgical procedures, but also to avoid battery malfunctioning (currently around 20%) [11]. Hence, promising energy harvesting technologies are those that will support long-term and intensive monitoring and actuation operations, processing of dynamic control and complex artificial intelligence algorithms, as well as short periods for data transmission/receiving [12-14]. Concerning large-scale powering, huge challenges must be addressed: even though the average annual consumption growth rate is estimated to surpass 1% per year up to 2050 [15], 90% of conventional non-renewable energy sources must be reduced over the next three decades, such that the global temperate rise keep below 2°C [16, 17]. Many relevant advances have been carried out in renewable energy systems [18-20]. Even so, they are not enough to overcome the limitations of intermittency of some renewable sources, such as wind and sun, and/or the significant time-varying mechanical excitations provided by wind and ocean energy, among others sources [21, 22]. If energy sources are intermittent, energy production costs are high, as complex grid management, expensive energy transduction mechanisms and energy storage systems are required [23]. If energy generators are designed to generate energy from non-intermittent sources: (1) high maintenance costs must be supported, as their energy transduction systems requires complex machinery (such as turbines, oleo-hydraulic systems and transmission systems); (2) low generation performance is obtained, as current non-intermittent renewable energy systems are not able to carry out performance adaptation to varying mechanical excitations [24, 25].

Many transduction mechanisms have been developed to convert the ubiquitous mechanical energy surrounding us to electric energy, among which one must highlight the piezoelectric [26, 27], electromagnetic [1, 28], and triboelectric [3, 29]. Electromagnetic harvesting is a unique technology because it is scalable from small- to large-scale [29-31]. Unlike triboelectric and piezoelectric harvesting, electromagnetic harvesters behave as low voltage sources with low internal impedance and high short-circuit currents [24, 32], which is essential to provide self-powering ability for a wide range of devices [28]. Moreover, electromagnetic energy harvesting systems using magnetic levitation architectures are recent disruptive technologies with a non-complex design that require low maintenance costs and provide stable performance over long harvesting time [28]. Although these are prominent features, this work claims that the most useful one is self-adaptability: so that their architectures can be automatically tuned to optimize the harvester length as a function of time-varying external power source dynamics driving the harvesters. This feature is of utmost importance as these electromagnetic harvesters exhibit highly nonlinear behaviors with resonant (excitation frequency matching the natural harvester resonance frequency) and hysteretic dynamics [24, 33]. Indeed, the geometric optimization prior to fabrication is by far not sufficient to ensure optimized performance throughout their operation. The problem remains critical even if alternative designs are used, such as multimodal architectures (array assemblies, i.e. chain or network of resonant structures), multi-stable architectures (n-stable harvesters) or hybrid architectures (such as electromagnetic-triboelectric generators) [30, 34-36]. In this paper, we propose an instrumented electromagnetic generator (EMG) for optimized self-adaptive performance. Instrumentation comprises: (i) an accelerometer to monitor the mechanical excitations driving the harvester; (ii) a stepper motor to change the harvester length by changing the distance between non-levitating magnets; (iii) a processing system with a microcontroller and conditioning circuitry to manage and control the entire system. We demonstrate here that this self-adaptive instrumented electromagnetic harvester provides significant performance gains. Successful simulation and experimental results will most likely trigger the development of a new era of highly sophisticated energy harvesters that are urgently required for emerging hybrid technologies.

2. Results

2.1 Structural design overview. An EMG prototype was developed comprising a hollow cylindrical structure, two multi-layer coils connected in series and three cylindrical annuli hard-magnetic elements, with a central stacked levitating-magnet experiencing levitation by opposite poles facing each other. Instrumentation was incorporated within the EMG for adaptive performance by controlling the distance between fixed magnets as a function of time-varying patterns of mechanical power sources externally exciting the harvesters. This instrumented harvester includes an accelerometer, a microcontroller, and a step motor to axially move one of the non-levitating magnets to an optimal position, by means of an open-

loop control system, as illustrated in Fig. 1a-e. The aperture parameter describes the distance between the fixed magnets, ranging between 0 and 40 mm, corresponding to distances between 60 and 100 mm, as shown in Fig. 1c. The levitating stack dynamics was also monitored using an ultrasonic sensor by measuring the axial distance to the tip of a thin inertial guiding rod coupled to the magnet. Overall, the simple linear shaped generator permits a straightforward optimization of the relative position between levitating-magnet and coils for maximum magnetic flux change. Two separate coils were used to maximize the effective electromechanical (EM) coupling with the levitating-magnet over all of its axial positions. A relatively large number of windings for the coils was employed to enhance the output energy conversion efficiency and voltage.
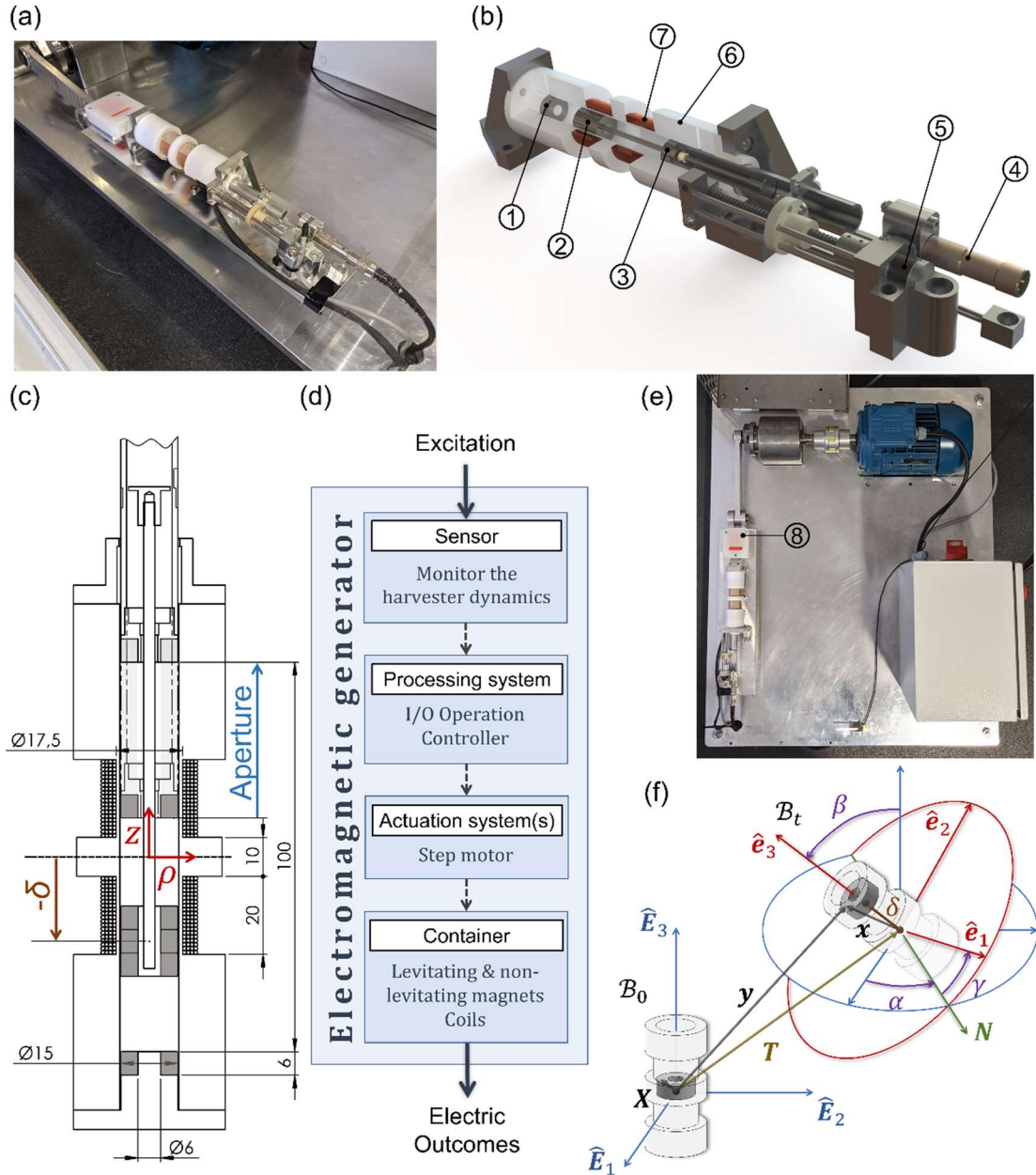

Fig. 1: (a) Instrumented harvester photo; (b) Photo-realistic view (1 – non-levitating magnet; 2 – levitating-magnet; 3 – adaptive non-levitating magnet; 4 – ultrasonic sensor; 5 – actuating stepper motor; 6 – container; 7 – coil); (c) Cross-sectional view; (d) Diagram representing the open-loop control approach using data from the mechanical excitation dynamics; (e) Custom experimental platform and adaptive electromagnetic energy harvester (8 – accelerometer and microcontroller); (f) Translations and rotations of the cylindrical container and levitating-magnet ($\mathcal{B}_t$), in relation to a time-independent reference configuration ($\mathcal{B}_0$), in inertial and non-inertial frames.

2.2 Model from first principles. The fundamental operation of levitating EMGs is based on the phenomenon of electromagnetic induction or the generation of an electromotive force in a wire loop by a changing magnetic flux from a moving magnet. According to Lenz's law, the generated electric currents produce magnetic fields opposing the change of the magnetic flux, thus providing a force opposing its relative motion (i.e., damping) by the conservation of momentum. Therefore, the generators convert part of the kinetic energy of its moving parts into electrical energy in the form of currents and voltages in an external circuit. The relationship between EM parameters can be derived using classical electrodynamics and rigid body dynamics, most generally described by Maxwell's equations, Lorentz force and balance laws for mass, momentum, and energy [24].

As shown in Fig. 1f, we consider a cylindrical material system to model the transduction mechanism of the EMG, whose points in a reference configuration are described in an inertial frame, with Cartesian coordinates and basis vectors $\hat{E}_I$ centered at the geometric center of the cylinder ($\hat{E}_3$ pointing along the rotational axis of symmetry), by the time-independent position vector X. In a time-dependent frame with orthonormal basis vectors $\hat{e}_i(t)$, also centered at the geometric center of the cylinder, which follows its movement in space, the current position of the reference point is given by $x = \chi(X, t)$. The basis vectors can be related through a R unitary rotation matrix (using Einstein's summation convention: upper case indexes for the vector components in the inertial frame and lower case indexes for the components in the non-inertial frame): $\hat{e}_i(t) = R_{iI}(t)\hat{E}_I$. The current position coordinates in each referential system are thus related by:

$$y_I = R_{iI}x_i + T_I,\qquad(1)$$

where $T(t)$ is a translation vector. Assuming the levitating-magnet as a rigid body constrained to unidimensional translations in the $\hat{e}_3$ direction, the points in its interior can be described by:

$$x_i = \delta_{iJ}X_J + \delta_{i3}\delta,\qquad(2)$$

where δ is the displacement, i.e. the axial position of the geometric center of the levitating-magnet in relation to the center of the container ($\int X_J dV_X = 0$, by definition), and δ_{iI} is the Kronecker delta symbol. Combining these two expressions with the balance of linear momentum equation for a rigid body in the inertial frame ($\int \rho_{density}\ddot{y}dV_X = F$) results in:

$$R_{iI}\left(\ddot{T}_I + (R_{3I}\ddot{\delta}) + (R_{iI}\ddot{\delta}_{iJ})X_J^{CM}\right) = F_i/m,\qquad(3)$$

where X_J^{CM} is the center of mass of the levitating-magnet (and guiding rod) in the reference configuration, F_i are the components of the external forces and m is the magnet mass. Expressing the rotation matrix in terms of intrinsic $z-x'-z''$ Euler angles α, β, γ to describe the container position in space at a given time (Fig. 1f) and assuming the center of mass position is along $\hat{E}_3$: $X_J^{CM} = \delta_{3J}X_3^{CM}$, simplifies the dynamic equation in the axial $i = 3$ direction to:

$$m\ddot{\delta} = F_3 + {}^{Inert}F_3 \qquad(4a)$$

$${}^{Inert}F_3 = m[-\cos(\beta)\delta_{3I}\ddot{T}_I + \sin(\beta)\cos(\alpha)\delta_{2I}\ddot{T}_I - \sin(\beta)\sin(\alpha)\,\delta_{1I}\ddot{T}_I + \left(\dot{\beta}^2 + \sin^2(\beta)\,\dot{\alpha}^2\right)(\delta + X_3^{CM})], \qquad(4b)$$

where ${}^{Inert}F_3$ is the equivalent inertial force applied to the levitating-magnet. In operation, external forces applied to the container (${}^{Ext}F_I = M\ddot{T}_I + F_I$, with M the mass of the container) compels it to move in space and, in the non-inertial frame of reference of the container, the levitating-magnet is subjected to resulting inertial forces [28, 37, 38]. The form of this force (equal to $-\hat{e}_3.\,m[\ddot{T} + \omega \times (\omega \times \hat{e}_3(\delta + X_3^{CM}))]$), in vector form with material angular velocity ω with components $\omega_j = (1/2)\varepsilon_{ijk}R_{iI}R_{kI}$; $\omega_J = -(1/2)\varepsilon_{IJK}R_{iI}\dot{R}_{iK}$), shows that the transduction system is sensitive to accelerations of the translation components along the axial direction of the cylinder ($\ddot{T}.\hat{e}_3$), as well as to time changes in precession (α) and nutation (β) angles, which are related to the centrifugal acceleration. The levitating-magnet is also allowed to undergo self-rotations by an angle θ around the $\hat{e}_3$ axis of the container in Eq. (2), so that $\gamma \to \gamma + \theta$, although this should not contribute to the output of the system as can be seen from the absence of the γ angle in Eq. (4b). The total axial force term (F_3) in the non-inertial referential does not contain components from normal tractions, which constrain the magnet to move inside the container, but includes

non-linear magnetic restoring forces ($^{Mag}F(\delta)$), gravity forces ($^{Grav}F(\beta)$), Lorentz braking forces ($^{Lrz}F(\delta, I)$) and mechanical damping forces ($^{Damp}F(\dot{\delta})$).

First principle models for EMGs make fundamental use of the quasi-magnetostatic form of the Maxwell's equations ($\partial \boldsymbol{D}/\partial t \approx 0$), Lorentz's force and continuum mechanics [39-41]. The magnetic fields, magnetic force between magnets and Lorentz forces between current loops and magnets can be obtained using equivalent surface current (Ampère model) [42, 43] or charge (Gilbert model) [43, 44] models or, alternatively, magnetic energy variation [28, 45] or Maxwell's stress tensor methods [46, 47]. Here we make use of the equivalent surface current model since it provides a similar formalism for the description of the magnetic fields generated by the magnets and coils.

Because the system under study has cylindrical symmetry, it is convenient to work in cylindrical coordinates (ρ, φ, z) with $\hat{\boldsymbol{e}}_z = \hat{\boldsymbol{e}}_3$, $\hat{\boldsymbol{e}}_\rho = \cos\varphi\,\hat{\boldsymbol{e}}_1 + \sin\varphi\,\hat{\boldsymbol{e}}_2$ and $\hat{\boldsymbol{e}}_\varphi = -\sin\varphi\,\hat{\boldsymbol{e}}_1 + \cos\varphi\,\hat{\boldsymbol{e}}_2$. For this special case, the magnetic fields and forces can be analytically computed using elliptic integrals [28, 48, 49] or Bessel functions [28, 50]. Considering a cylindrical annuli shaped permanent magnet with a constant magnetization pointing in the $\hat{\boldsymbol{e}}_z$ direction, $\mathbf{M} = M_z \hat{\boldsymbol{e}}'_z$ ($\nabla' \times \mathbf{M} = 0$; $\boldsymbol{J}_f = 0$), occupying a volume described by $^Mz - {}^ML/2 \leq z' \leq {}^Mz + {}^ML/2$; $^M\rho_I \leq \rho' \leq {}^M\rho_O$; $0 \leq \varphi' < 2\pi$, where ^Mz is the z position of its center in the symmetry axis, ^ML its length, $^M\rho_I$ the inner radius and $^M\rho_O$ the outer radius. With the quasi-magnetostatic Maxwell equations and Helmholtz decomposition theorem for the magnetic induction $\boldsymbol{B} = \nabla \times \boldsymbol{A}$ field ($\mathbf{A} = (\mu_0/4\pi)\left(\int_V dV'\left(\boldsymbol{J}_f + \nabla' \times \mathbf{M}\right)/|\boldsymbol{x} - \boldsymbol{x}'| + \int_A (\mathbf{M} \times d\mathbf{A}')/|\boldsymbol{x} - \boldsymbol{x}'|\right)$, where μ_0 is the vacuum permeability), and element of area $d\mathbf{A}' = \{\pm\hat{\boldsymbol{e}}'_z\rho'\,d\varphi'\,d\rho', \text{for } z' = {}^Mz \pm {}^ML/2; \pm\hat{\boldsymbol{e}}'_\rho\rho'\,d\varphi'\,dz', \text{for } \rho' = {}^M\rho_O, {}^M\rho_I$, the only non-null component of the magnetic vector potential is:

$$^M A_\varphi(\rho, z) = \frac{\mu_0 M_z}{2\pi} \left.\int_{M_z - \frac{M_L}{2}}^{M_z + \frac{M_L}{2}} dz' f(\rho, z, \rho', z')\right]_{\rho' = {}^M\rho_I}^{\rho' = {}^M\rho_O} \tag{5a}$$

$$f(\rho, z, \rho', z') = \int_0^\pi d\varphi' \frac{-\rho'\cos(\varphi')}{\sqrt{\rho^2 + \rho'^2 + 2\rho\rho'\cos(\varphi') + (z-z')^2}}, \tag{5b}$$

where $f(\rho, z, \rho', z')$ is an important dimensionless function which can be written in terms of complete elliptic integrals of the first and second kind ($f = (\beta/2\rho)[(2 - k^2)K(k) - 2E(k)]$; $k^2 = 4\rho\rho'/\beta^2$; $\beta^2 = (\rho + \rho')^2 + (z - z')^2$) [28] and has the useful commutation properties: $f(\rho, z, \rho', z') = f(\rho, z', \rho', z)$, $\rho . f(\rho, z, \rho', z') = \rho' . f(\rho', z, \rho, z')$, $\partial_z f(\rho, z, \rho', z') = -\partial_{z'} f(\rho, z, \rho', z')$. Fig. 2a shows the distribution of this magnetic vector potential in space for the EMG.

The other component of the system is a coil which for simplicity we assume to be composed of infinitesimally thin current loops with a radius $^I\rho$ and axial position ^Iz. The corresponding free-current density is: $\boldsymbol{J}_f = \hat{\boldsymbol{e}}'_\varphi I\delta(\rho' - {}^I\rho)\delta(z' - {}^Iz)$, where I is the current and $\delta()$ are Dirac delta functions. The same procedure yields the magnetic vector potential for a single loop of wire ($\mathbf{M} = 0$):

$$^I A_\varphi(\rho, z) = \frac{\mu_0 I}{2\pi} f(\rho, z, {}^I\rho, {}^Iz). \tag{6}$$

The distribution of this vector potential is depicted in Fig. 2c for the two coils connected in series per unit of flowing current, producing a force that tends to push the levitating-magnet downwards. The two non-null components of the magnetic fields can be obtained from the two potentials (defined by Eqs. (5a) and (6)) by: $B_z = (1/\rho)\partial_\rho(\rho A_\varphi)$, $B_\rho = -\partial_z A_\varphi$, and are represented in Fig. 2b,d. From the superposition principle, the total magnetic field associated with the system is the sum of each component due to the magnets and current loops. Thus, for N_M magnets and N_I current loops, the total magnetic vector potential at a given point in space is given by: $A_\varphi(\rho, z) = \sum_{j=1}^{N_I} {}^{I_j}A_\varphi(\rho, z, {}^{I_j}\rho, {}^{I_j}z) + \sum_{k=1}^{N_M} {}^{M_k}A_\varphi(\rho, z, {}^{M_k}\rho_O, {}^{M_k}\rho_I, {}^{M_k}z, {}^{M_k}L)$. For a large number of current loops, the summation can be approximated by a continuous integration with a given density of loops.

From Faraday's law of induction, we can model, in integral form, the generation of an electromotive force (ξ) in a current loop from the time change of the magnetic flux (Φ_B) over a time-independent surface delimited by the current path ($\xi = -d\Phi_B/dt$). If we consider the surface with area element $d\boldsymbol{A} = \hat{\boldsymbol{e}}_z\rho\,d\varphi\,d\rho$, and the magnetic fields calculated before with projected magnetic field component B_z, we find

$\Phi_B = 2\pi {}^I\rho A_\varphi({}^I\rho, {}^Iz)$, and the total electromotive force induced on a loop i by the time changing currents (I_j), flowing on other loops (with index j), and the displacement of the levitating-magnet (δ) is:

$$\xi_i = -L_{ij}\dot{I}_j - {}^{EM}\alpha_i\dot{\delta} \tag{7a}$$

$$ {}^{EM}\alpha_i = \partial^i\Phi_B/\partial\delta = \mu_0 M_z {}^{I_i}\rho f\left({}^{I_i}\rho, {}^{I_i}z, \rho', z'\right)\Big]_{z'=\delta-\frac{M_L}{2}}^{z'=\delta+\frac{M_L}{2}}\Big|_{\rho'={}^M\rho_I}^{\rho'={}^M\rho_O} \tag{7b}$$

$$L_{ij} = \partial^i\Phi_B/\partial I_j = \mu_0 {}^{I_i}\rho f\left({}^{I_i}\rho, {}^{I_i}z, {}^{I_j}\rho, {}^{I_j}z\right) = L_{ji}, \tag{7c}$$

where L_{ij} is the inductance matrix of the coil and ${}^{EM}\alpha_i$ is an EM coupling factor between magnets and coil loops, which relates the output voltage with the velocity of the magnet. As shown in Fig. 2e, this coefficient takes maximum absolute values (with different signs) when the top or bottom edge of the levitating-magnet is at the center position of a loop of wire with the same radius (i.e. where the change of magnetic flux for a given axial infinitesimal displacement is maximal) [42, 51]. Therefore, these are the regions where the loops of the coil should be concentrated, up to a certain radius where the contribution to the internal resistance of the coil becomes more significant than the contribution to the EM coupling. As the length-to-radius ratio of the magnet increases, the regions with high magnetic flux change reach farther away in the radial direction and the average absolute EM coupling over all of space increases up to a maximum value (up to length-to-radius of ≈ 3, after which staked magnets with opposite magnetizations, such as in Ref. [38], and the same total length can start to become practical). The self-inductance terms L_{ii} in Eq. (7c) diverge, because the loops were assumed to be infinitely thin, but Eq. (7c) can still be used to estimate its value, such as by calculating the magnetic flux through the outer or inner parts of loops with a finite wire diameter Φ.
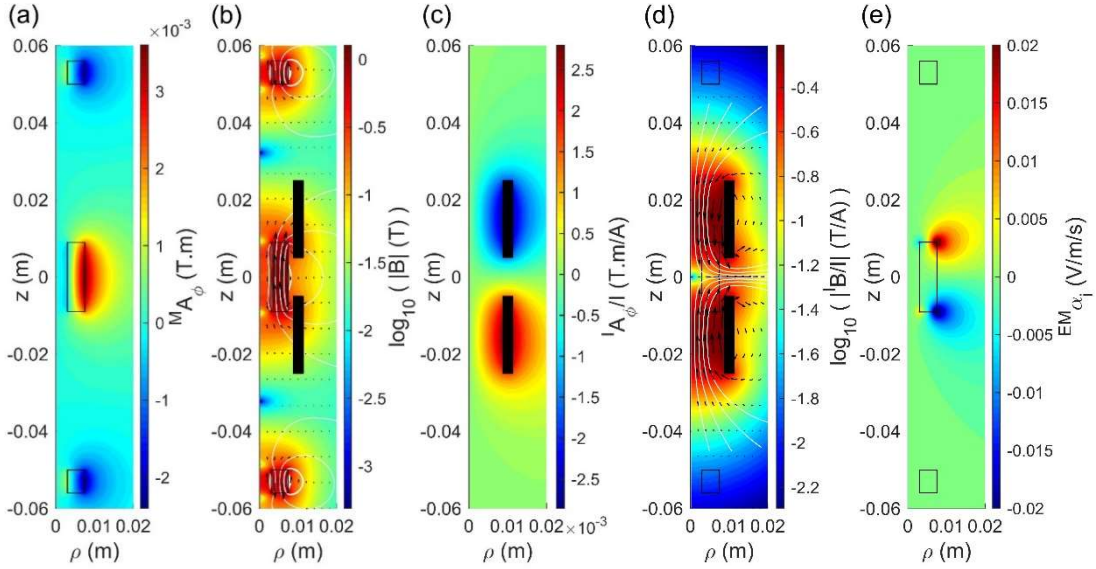

Fig. 2: (a) Magnetic vector potential and (b) corresponding magnetic induction field (field lines (in white) and direction arrows (in black) and corresponding absolute value in color scale) generated by the magnets; (c) Magnetic vector potential and (d) corresponding magnetic induction field generated per unit of current flowing through the coils; (e) Variation of the magnetic flux (Φ_B) through a centered loop of wire (at position z with radius ρ) with the variation of the vertical position of the levitating-magnet (δ), equivalent to the electromechanical coupling factor $({}^{EM}\alpha_i)$ for a single loop.

With Maxwell-Faraday's equation, Ohm's law and Kirchhoff's circuit laws, connecting the N_I loops of the coil in series (described by an array $(\pm1)_i$, with $+1$ and -1 as array elements, depending on which terminals + and - are connected to which other) to an external circuit, yields a total voltage $V = \sum_{i=1}^{N_I}(\pm1)_i V_i$ and current $I = (\pm1)_i I_i$ (with no summation over i) related by:

$$V = -R_I I - L_I\dot{I} - {}^{EM}\alpha\dot{\delta} \tag{8a}$$

$$^{EM}\alpha = \sum_{i=1}^{N_I} (\pm 1)_i \, ^{EM}\alpha_i \tag{8b}$$

$$L_I = \sum_{i=1}^{N_I} \sum_{j=1}^{N_I} (\pm 1)_i L_{ij} (\pm 1)_j, \tag{8c}$$

where $^{EM}\alpha$ is the total EM coupling coefficient [37, 42, 52], roughly increasing with the number of loops of the coil, R_I is the inner equivalent resistance of the coil and L_I is its equivalent inductance. The EM coupling coefficient, unlike considered in most studies where it tends to be averaged out [24, 28, 37, 38, 45, 52], strongly depends on the relative position between the levitating-magnet and coils, significantly influencing the form of the system's output. As shown in Fig. 3a, this coefficient for two different coils appropriately connected in series is the sum of the coefficient related to each coil. A maximum absolute value is reached when the magnet has its two vertices in the interior region of each of the coils. A null value occurs when the magnet is completely inside a single coil since the changes in magnetic flux in each loop cancel out. A second local maximum occurs for larger displacements when only one of the vertices is inside a single coil. The EM coupling curve for a single loop of wire has a symmetric shape (i.e. an odd function) similar to the one for a single coil shown in Fig. 3a (bottom or top), centered at the axial $^I z$ position of the loop and with thinner positive and negative maximum peaks on the sides separated by a distance equal to the length of the levitating-magnet. Therefore, concentrating closely spaced loops of wire connected in series along the axial direction results in a linear superposition of the EM coupling factors (and resistances) and a corresponding increase and widening of the peaks up to a certain point. As the axial length of the coil starts to get closer to the length of the magnet, the individual positive and negative peaks begin to overlap and the EM peaks attain maximum absolute values. Since in general we aim to maximize a $^{EM}\alpha^2/R_I$ factor, relating the output power with the velocity of the levitating-magnet at a certain position, a configuration with multiple coils with lengths inferior to the length of the magnet connected in series in an alternate fashion is sought after. Regarding the axial length of the coils, a compromise must be found since lengths closer to the length of the magnet result in a maximum average of the $^{EM}\alpha^2/R_I$ factor over all of the δ magnet position space, while lower lengths might result in larger and thinner $^{EM}\alpha^2/R_I$ factor peaks, which can be useful for small amplitude excitations. A parallel connection between the coils can also be considered although in general yielding worst results due to the flow of currents between coils with large and low induced electromotive force instead of through the external circuit.

The Lorentz forces induced on an isolated material by an external magnetic field ($\mathbf{B_0}$) can be given in integral form by [41]: $^B\boldsymbol{F} = \int_V dV (\mathbf{J}_f + \boldsymbol{\nabla} \times \mathbf{M}) \times \mathbf{B_0} + \int_A dA (\mathbf{M} \times \hat{\mathbf{n}}) \times \mathbf{B_0}$. For the levitating-magnet ($\mathbf{J}_f + \boldsymbol{\nabla} \times \mathbf{M} = 0$), taking into account the cylindrical symmetry of the system ($dA(\mathbf{M} \times \hat{\mathbf{n}}) \times \mathbf{B_0} = \left\{ \pm \rho d\varphi dz \left(-\hat{\boldsymbol{e}}_z M_z B_{0_\rho}(\rho, z) + \hat{\boldsymbol{e}}_\rho M_z B_{0_z}(\rho, z) \right) \right.$, for $\rho = \,^M\rho_O, \,^M\rho_I$), the non-null $\hat{\boldsymbol{e}}_3 = \hat{\boldsymbol{e}}_z$ directed component of the force applied to it will be:

$$^B F_3 = 2\pi M_z \rho A_{0_\varphi}(\rho, z) \Big]_{z=\delta-\frac{M_L}{2}}^{z=\delta+\frac{M_L}{2}} \Big|_{\rho=\,^M\rho_I}^{\rho=\,^M\rho_O}. \tag{9}$$

With the magnetic vector potentials associated with the fixed magnets given by Eq. (5a), the total magnetic restoring force applied to the levitating-magnet (with index $k = 1$) is:

$$^{Mag} F_3 = \sum_{k=2}^{N_M} M_z \mu_0 M_{zk} \rho \int_{M_{kz} - \frac{M_{kL}}{2}}^{M_{kz} + \frac{M_{kL}}{2}} dz' f(\rho, z, \rho', z')\Big]_{\rho' =\,^{Mk}\rho_I}^{\rho' =\,^{Mk}\rho_O} \Big]_{z=\delta-\frac{M_L}{2}}^{z=\delta+\frac{M_L}{2}} \Big|_{\rho=\,^M\rho_I}^{\rho=\,^M\rho_O}. \tag{10}$$

This integral can be evaluated using the elliptic integrals or by interchanging the order of integration and numerically solving the analytical result. This magnetic restoring force changes according to a highly non-linear pattern with the position of the levitating-magnet, as depicted in Fig. 3b, and is the symmetrical superposition of the magnetic forces from each individual fixed magnet, with the position of the top one depending on the value of the aperture. The angular natural frequency of the system ($\omega_0(\delta) = \sqrt{k/m} \approx 6$ Hz; $k = -\partial^{Mag} F_3(\delta)/\partial\delta$), where the output power is typically maximal, can be tuned by controlling the distance between fixed magnets (i.e. the aperture of the container) [42]. The calculated variation of the natural frequency of the system in its equilibrium position as a function of the aperture is shown in Fig. 3c, taking values between 6 Hz and 18 Hz and changing approx. with the –5/2 power of the distance between

magnets. The resonance frequency also tends to increase with the axial length of the levitating-magnet since, although the mass increases the slope of the magnetic restoring force increases faster.

The force Eq. (9), with the magnetic vector potentials associated with the current loops given by Eq. (6), results in the total Lorentz braking force applied to the levitating-magnet by the currents flowing in the loops:

$$^{Lrz}F_3 = \sum_{i=1}^{N_I} \mathrm{M}_z \mu_0 I_i \rho f(\rho, z, {}^{I_i}\rho, {}^{I_i}z)] \Big|_{\substack{z=\delta-\frac{M_L}{2} \\ \rho={}^M\rho_I}}^{\substack{z=\delta+\frac{M_L}{2} \\ \rho={}^M\rho_O}} = {}^{EM}\alpha I,$$

(11)

where the identity is due to the commuting properties of the f function and Eqs. (8b) and (7b). Close range Lorentz forces produced by eddy currents on the conductive Ni plating of the transversal faces of the NdFeB magnets were not taken into account.

The gravity force ($^{Grav}\boldsymbol{F} = -mg\hat{E}_3$) on the levitating-magnet in the axial direction can be approximated by:

$$^{Grav}F_3 = -mg\cos(\beta),$$

(12)

where g is the standard acceleration of gravity. This shows that the transduction system is also sensitive to changes in axial orientation in relation to Earth's gravitational field. The mechanical damping force term was modelled taking into account the Coulomb dry friction and viscous drag friction:

$$^{Damp}F_3 = \begin{cases} -^{In}F_3 & , |\dot{\delta}| = 0 \wedge |^{In}F_3| < \mu_s F_n \\ -\mu_s F_n \mathrm{sign}(^{In}F_3) & , |\dot{\delta}| = 0 \wedge |^{In}F_3| \geq \mu_s F_n, \\ -c\dot{\delta} - \mu_k F_n \mathrm{sign}(\dot{\delta}) & , |\dot{\delta}| > 0 \end{cases}$$

(13)

where $^{In}F_3$ is the total force applied to the levitating-magnet excluding the damping force itself, F_n is the normal force exerted by the walls of the container (equal to $mg.|\sin(\beta)|$ for translations along the axial direction), μ_s is the static coefficient of friction, μ_k the kinetic coefficient of friction and c the mechanical damping coefficient.
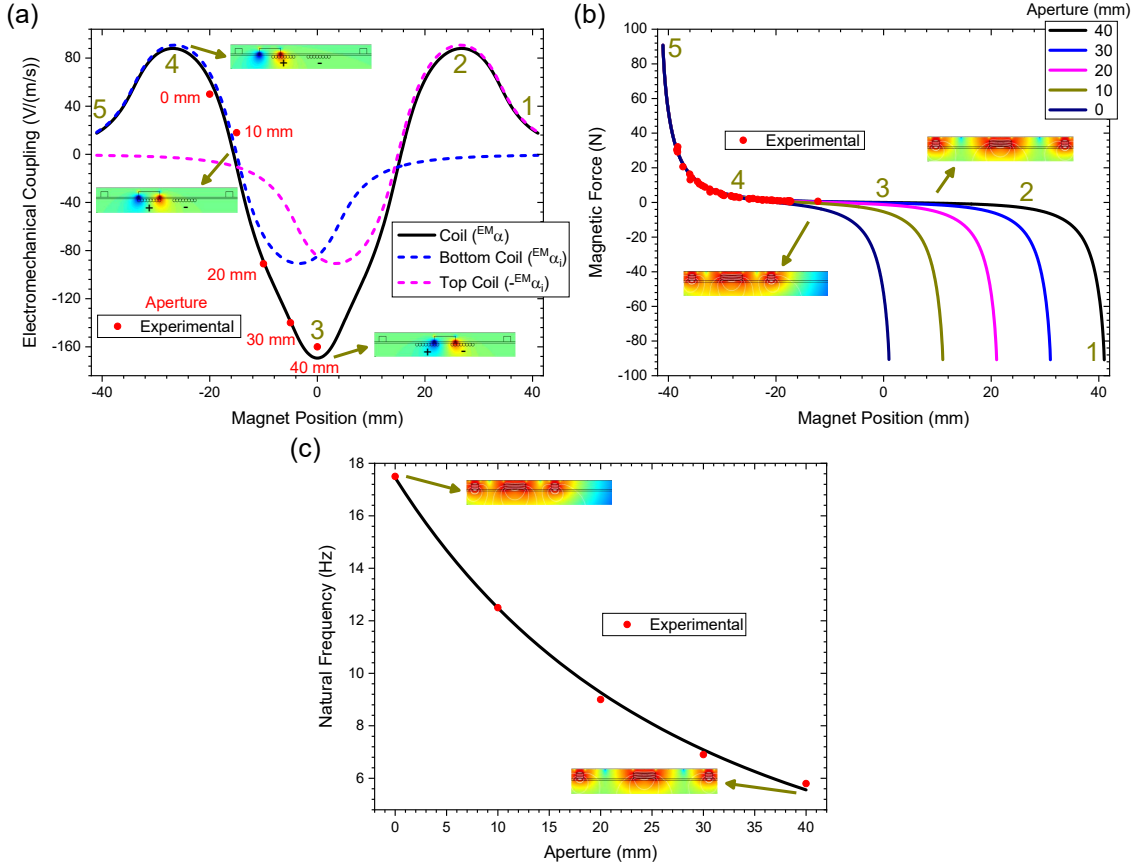
Fig. 3: (a) Electromechanical coupling coefficient calculated as a function of the levitating-magnet position (δ) for the two coils connected in series and for each separate coil. Equilibrium positions for each aperture and 1-5 position labels correspondent to those in Fig. 5 are indicated; (b) Variation of the magnetic restoring force applied to the levitating-magnet by the fixed magnets with its position for different apertures of the container. Experimentally determined values for the force between the bottom magnet and the levitating-magnet are shown; (c) Natural resonance frequency of the generator in the equilibrium position as a function of the aperture. Experimentally measured values are superimposed.

Combining the balance of the linear momentum, electrical circuit equations and forces, as provided by Eqs. (4a), (8a) and (10-13), a system of non-linear second-order ordinary differential equations (ODE) is obtained to completely describe the behavior of the generator:

$$\begin{cases} m\ddot{\delta} - {}^{EM}\alpha(\delta)I - {}^{Damp}F_3\left(\dot{\delta}, {}^{In}F_3\right) - {}^{Mag}F_3(\delta) = {}^{Inert}F_3(\boldsymbol{T}, \alpha, \beta, \delta) + {}^{Grav}F_3(\beta) \\ V + L_I\dot{I} + R_II + {}^{EM}\alpha(\delta)\dot{\delta} = 0 \end{cases}. \tag{14}$$

This system of equations can be solved for the displacement δ and current I as a function of time with prescribed initial conditions of displacement ($\delta(0) = \delta_0$), velocity ($\dot{\delta}(0) = \dot{\delta}_0$) and current ($I(0) = I_0$), provided relation between the voltage and current for the external circuit ($V = V(I)$), as well as the time-dependent input translation ($\boldsymbol{T}$) and rotation (α and β) components. In this study, a resistive load (R) is connected to the output of the coils, so that Ohm's law applies: $V = RI$. Multiplying the top equation in (14) by $\dot{\delta}$ and the bottom equation by I, and combining the terms results in a statement of conservation of energy i.e. the power input from the external inertial and gravity forces equals the power loss due to friction and Joule heating plus the time rate of change of the kinetic ($(1/2)m\dot{\delta}^2$), potential ($-\int {}^{Mag}F_3(\delta)d\delta$) and inductor ($(1/2)L_II^2$) energies. A low-frequency approximation can usually be considered, in which the $L_I\dot{I}$ term in the bottom equation is assumed to be small when compared to the other terms (i.e., for frequency of excitation $f \ll (R + R_I)/2\pi L_I \approx 327$ Hz) and, thus, the current can be written explicitly as [51]: $I = -{}^{EM}\alpha(\delta)\dot{\delta}/(R + R_I)$. This important expression shows that the output current of the generator will be approx. equal to the product of the EM coefficient at a certain position of the magnet and its corresponding velocity. The current in this form can then be plugged into the top equation in (14), resulting in a single second-order ODE with a load-dependent EM damping constant equal to: $c_{EM} = {}^{EM}\alpha(\delta)^2/(R + R_I)$. The magnetic force and EM coupling coefficient change in a highly non-linear manner with the position of the

9

levitating-magnet, so that approximate solutions to this kind of equation are commonly obtained analytically using a harmonic balance method or a perturbation method of multiple scales [52] or numerically e.g., using Runge-Kutta methods [28, 33, 53].

In a first approximation, valid for low enough displacements of the levitating-magnet, the magnetic force, and EM damping terms can be expanded in a power series around an equilibrium point of the system. Truncating the powers up to order one for the magnetic force ($\omega_0(\delta) \approx \omega_0$) and zero for the EM coefficient ($^{EM}\alpha(\delta) \approx {}^{EM}\alpha_0$), using a simple viscous force ($^{Damp}F_3 = -c\dot{\delta}$) and an input harmonic forcing term ($^{Inert}F_3 = m\omega^2 X\cos(\omega t)$ and $^{Grav}F_3 = 0$), with translation amplitude X, results in the linear driven harmonic oscillator equation with a well-known analytical solution [54]. The corresponding complex displacement phasor (i.e., for a complex exponential response formula $z = \hat{z}e^{i\omega t}$), current/voltage phasors and average output power are given by the following equations:

$$\hat{\delta} = X\frac{\omega^2}{(\omega_0^2 - \omega^2) + i\omega\omega_0 2(\zeta_M + \zeta_{EM})} \tag{15a}$$

$$\hat{I} = \frac{\hat{V}}{R} = -\frac{{}^{EM}\alpha_0}{R + R_I}i\omega\hat{\delta} \tag{15b}$$

$$\langle P \rangle = \frac{m}{\omega_0}(X\omega^2)^2\frac{R}{R + R_I}\zeta_{EM}\frac{(\omega\omega_0)^2}{(\omega_0^2 - \omega^2)^2 + \left(\omega\omega_0 2(\zeta_M + \zeta_{EM})\right)^2} \tag{15c}$$

$$\zeta_{EM} = \frac{{}^{EM}\alpha_0^2}{R + R_I}\frac{1}{2m\omega_0}, \quad \zeta_M = c\frac{1}{2m\omega_0}, \tag{15d}$$

where ζ_{EM} and ζ_M are effective EM and mechanical damping ratios, respectively. These equations show that all electrical parameters have a resonant behavior, taking local maximum absolute peak values for $\omega = \omega_0$. Besides, the displacement, voltage and current increase linearly with the displacement amplitude (X), while the average power increases with its square. Larger values of the load resistance (R) also correspond to smaller EM damping ratio (ζ_{EM}) and, thus, larger resonant displacements and sharper peaks. The linear EMG behaves broadly like a Thévenin (Norton) equivalent circuit composed of a voltage (current) source, with amplitude $\hat{V}_{OC}$ ($\hat{I}_{SC}$) given by Eq. (15b) in the limit of an infinite (null) load resistance R, and an internal complex impedance in series (parallel) given by the ratio $Z = \hat{V}_{OC}/\hat{I}_{SC}$. The output average power should be of the form $\langle P \rangle = (1/2)RII^*$, taking a maximum value of $\langle P \rangle_{Max} = (1/4)|\hat{V}_{OC}||\hat{I}_{SC}|(|Z|/[|Z| + Z'])$ for an optimal matching resistance $R = |Z| = |\hat{V}_{OC}|/|\hat{I}_{SC}|$ (the asterisk indicates the complex conjugate and the apostrophe the real part). This resistance is approx. equal to the internal resistance of the coil for sufficiently low and high frequencies. For frequencies significantly larger than the resonant frequency, the maximum average power takes a value of $\langle P \rangle_{Max,\omega \gg \omega_0} = (X\omega)^2(1/8)({}^{EM}\alpha_0^2/R_I)$, increasing with the square of the frequency. Thus, maximum average powers are generally expected for conditions of maximum amplitude and frequency, while also being limited by the maximum displacement amplitude allowed for each aperture ($|\hat{\delta}|_{Max} = 21 + (1/2)Aper$, where $Aper$ is the aperture in mm). Under resonance conditions ($\omega = \omega_0$), the matching resistance takes a maximum value that can be as large as $R_{\omega=\omega_0} = R_I + {}^{EM}\alpha_0^2/c = R_I(1 + \zeta_{EM0}/\zeta_M)$, with $\zeta_{EM0} = {}^{EM}\alpha_0^2/R_I 2m\omega_0$ [54]. The corresponding maximum average power increases with the $mX^2\omega_0^3$ power factor and approx. with the inverse of the mechanical damping ratio ζ_M (up to an upper limit due to physical constrains and the steady-state never being achievable for $\zeta_M \to 0$) as $\langle P \rangle_{Max,\omega=\omega_0} = (mX^2\omega_0^3)(1/8)(1/2\zeta_M)(\zeta_{EM0}/[\zeta_{EM0} + \zeta_M])$. The energy conversion efficiency over one cycle of period T in the steady-state can be given by: $\eta = \int_0^T VIdt / \int_0^T -({}^{Lrz}F_3 + {}^{Damp}F_3)\dot{\delta}dt = R\zeta_{EM}/(R + R_I)(\zeta_{EM} + \zeta_M)$, taking a maximum value at $R = R_I\sqrt{1 + (\zeta_{EM0}/\zeta_M)}$ of $\eta_{Max} = (\zeta_{EM0}/\zeta_M)^{-1}\left((\zeta_{EM0}/\zeta_M) - 2\sqrt{1 + (\zeta_{EM0}/\zeta_M)} + 2\right)$, increasing from 0 to 1 with the ζ_{EM0}/ζ_M ratio. The ${}^{EM}\alpha_0^2/R_I$ factor, is thus a good indicator of the ability of the system to convert kinetic energy into electrical energy, scaling roughly with the number of loops in the coil, the radius and the square of the magnetization of the levitating-magnet. Scaling each dimension of the EMG by a constant C term, while maintaining the aspect-ratio, will result in the transformations ${}^{EM}\alpha(\delta) \to C.{}^{EM}\alpha(\delta/C)$, ${}^{Mag}F_3(\delta) \to C^2.{}^{Mag}F_3(\delta/C)$, $\omega_0 \to C^{-1}.\omega_0$, $m \to C^3.m$, $R_I \to C.R_I$, and corresponding average powers normalized by the square of the acceleration ($\omega^2 X)^2$ for a matching load scaling with C^5, at low frequencies, C, at large frequencies, and approx. between C^6 and C^4 under resonance conditions, depending on whether the mechanical damping constant will scale as C^0 or C^2.

In the general case, Eq. (14) is more similar to Duffing's differential equation with a cubic nonlinearity [52, 55] exhibiting a hardening stiffness, with the frequency response overhanging to the high-frequency

side as well as a hysteretic response, with two solutions for frequencies close to the resonance frequency, as well as amplitude jumps at two points. Furthermore, the non-linearity of the EM coefficient also results in higher harmonic output electrical signals with characteristic frequencies at multiples of the input frequency, each one initially increasing proportionally with higher powers of the input amplitude (i.e. $I = (1/2)[(\hat{I}_1 e^{i\omega t} + \hat{I}_1^* e^{-i\omega}) + (\hat{I}_2 e^{i2\omega} + \hat{I}_2^* e^{-i2\omega t}) + (\hat{I}_3 e^{i3\omega} + \hat{I}_3^* e^{-i3\omega}) + \cdots]$, with $\hat{I}_1 = I'[^{EM}\alpha\hat{\delta} + \cdots]$, $\hat{I}_2 = I'(1/2)[(\partial^{EM}\alpha/\partial\delta)\hat{\delta}^2 + \cdots]$, $\hat{I}_3 = I'(1/8)[(\partial^{2EM}\alpha/\partial\delta^2)\hat{\delta}^3 + \cdots]$; $I' = -i\omega(R + R_I)^{-1})$. When the position of equilibrium of the levitating-magnet is centered between the two coils, for the maximum aperture of 40 mm, the EM coupling is an even function of the position corresponding to non-null even derivatives. Thus, the system has dominant output voltages with the same frequency as the input signal or odd multiples of it for large enough amplitudes of excitation. When the equilibrium position is centered on a single coil, as occurs for an aperture of 10 mm, the EM coupling is locally an odd function of the position corresponding to large odd derivatives. The generator thus will provide dominant output voltages at even multiples of the frequency of the input.

In this study, we considered simple translations of the EMG along its axial direction with a sinusoidal time-changing inertial force, as exhibited in Eq. (4b), with the following parameters: $\alpha = 0$; $\beta = -\pi/2$; $T_1 = T_3 = 0$; $T_2 = X\cos(\omega t)$; $^{Inert}F_3 = m\omega^2 X\cos(\omega t)$. The initial conditions were set to: $\delta(0) = \dot{\delta}(0) = I(0) = 0$. The time and frequency response of the transduction mechanism was investigated with a constant amplitude of displacement X, while continuously sweeping the frequency ω in steps in ascending followed by descending order. The differential Eq. (14) was numerically solved using Runge-Kutta methods. The tested parameters of excitation of the system, as well as its EM characteristics, are summarized in Table 1.

Table 1 – Parameters of excitation and electromechanical characteristics of the generator.

Frequency (Hz)	Amplitude (mm)	Resistance (Ω)	Aperture (mm)	$^M z$ (mm)	$^M L$ (mm)	$^M \rho_I$ (mm)	$^M \rho_O$ (mm)	m (g)	$\mathbf{M_z}$ (MA/m)
4−18	3−10	1k−5M	0−40	-53/δ /13−53	6/ 18/ 6	3	7.5	28.26	1.138
$^I z_L$ (mm)	$^I \rho_L$ (mm)	Φ (μm)	$N_L \times N_P$	R_I (kΩ)	L_I (H)	c (N/(m/s))	μ_s	μ_k	(± 1)
$\pm 5 \pm \Phi/2$	$8.75 + \Phi/2$	67	298×45	8.41	4.1	0.31	0.04	0.04	[1, −1]

The computed frequency response of the generator, with an aperture of 20 mm, for a low amplitude of excitation of $X = 3$ mm and various load resistances, is shown in Fig. 4. For low values of the resistance (< 50 kΩ), the generator behaves as predicted by the linear approximation given by Eqs. (15a-d). At low and high frequencies, the output average power is maximal for a matching load approx. equal to the internal resistance of the coil. Under resonance conditions at ≈ 9 Hz, the amplitude of displacement, velocity, and voltage are enhanced, and the average power has a local maximum for an optimal load of $R_{\omega=\omega_0} = R_I + {}^{EM}\alpha_0^2/c \approx 34$ kΩ. For loads between 50 kΩ and 350 kΩ, the effective EM damping ratios (ζ_{EM}) are small, resulting in larger displacements where the non-linearities of the force and EM constant become noticeable. The characteristic shifting of the resonant frequency to higher values and hysteresis can be observed. Since the amplitude of the input displacement is kept constant, the corresponding acceleration increases very rapidly with the frequency as $\omega^2 X$. Therefore, as depicted in Fig. 4, a permanent stable non-linear resonant steady-state may appear very suddenly after a threshold of sufficiently large frequency, amplitude, and resistance (> 350 kΩ in this case). This state is characterized by levitating-magnet displacement amplitudes very close to the maximum allowed displacements, as well as by high velocities and voltages up to large frequencies. Rather than having a hysteretic response, this non-linear resonance is dependent on the initial conditions (as it is detailed in the following section). Even though the linear natural resonance frequency is 9 Hz, the maximum output average power is observed at a frequency of 18 Hz under non-linear resonance conditions for an optimal load that can be as large as 500 kΩ (Fig. 4d). The insets in Figs. 4a-c show the characteristic phase lag of the output ($\theta = \text{atan2}(-\hat{z}'', \hat{z}')$, for an output function approx. of the form $|\hat{z}|\cos(\omega t - \theta)$), indicating that the displacement of the levitating-magnet is in phase with the input excitation for low frequencies and 180º out-of-phase for large frequencies. Close to the resonance frequency, it takes values of the order of 90º. The energy conversion efficiency can increase up to ≈ 40% for a load of 20 kΩ, as depicted in the inset of Fig. 4d.
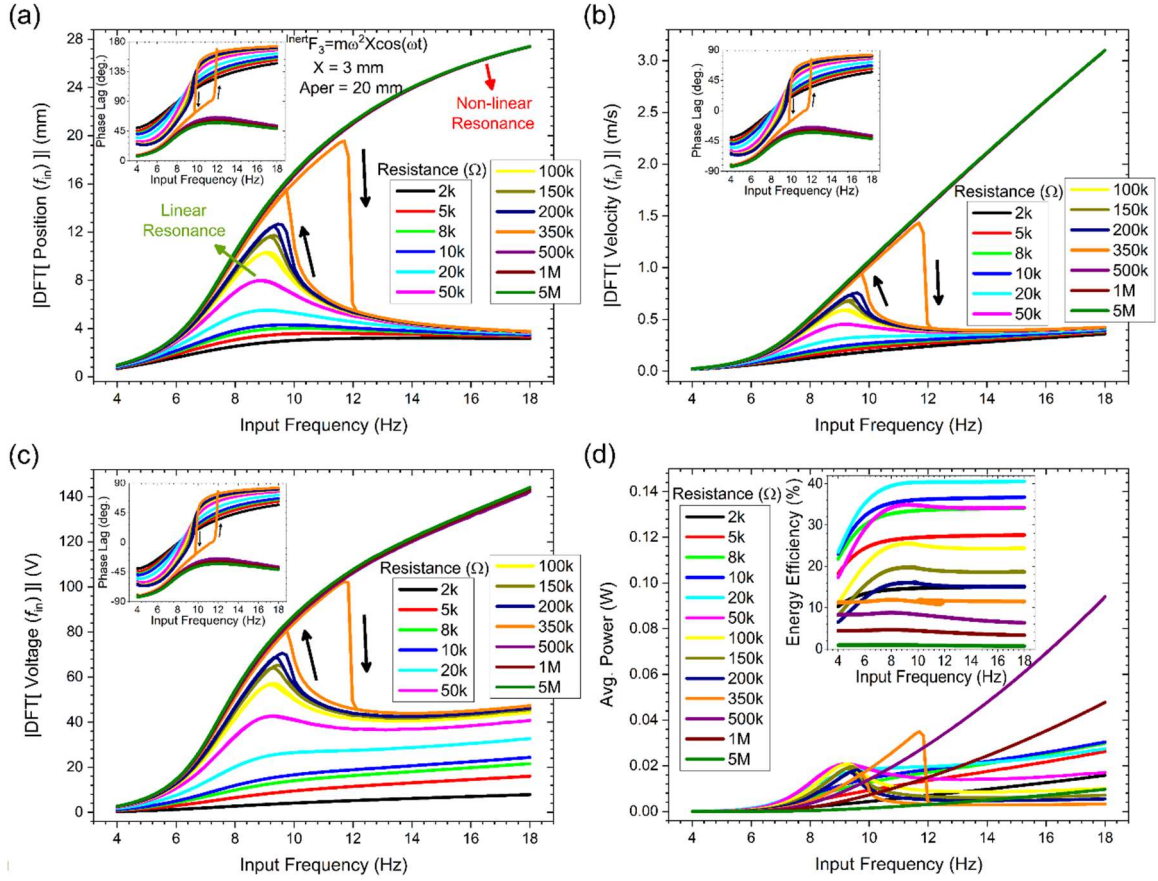
Fig. 4: Frequency response of the EMG (aperture of 20 mm) to a harmonic translational input with low amplitude X = 3 mm for different load resistances. Discrete Fourier transforms (component with the same frequency as the frequency of the input signal) of the output: (a) position of the levitating-magnet; (b) velocity of the levitating-magnet; and (c) voltage. The insets show the corresponding phase lag. (d) Output average power. The inset shows the energy conversion efficiency.

The calculated time response of the EMG is shown in Fig. 5a-d. It was obtained for a maximum aperture of 40 mm, a large amplitude of excitation of X = 10 mm and frequency of f = 18 Hz, and an optimal load resistance of 30 kΩ. Depending on whether the generator behavior was conducted to reach these conditions from high initial displacement/velocity, as in the frequency sweep case, or from rest, it may evolve into a non-linear resonant high amplitude or a non-resonant lower amplitude steady state. As highlighted by Fig. 5, the characteristic times of the transient responses are low. Under high-frequency resonant conditions, the output displacement and velocity of the levitating-magnet, shown in Fig. 5a,b, have almost triangular and rectangular waveforms, respectively, a scenario in which the Lorentz braking force acts with low relative significance. The correspondence between the displacement/velocity (Fig. 5a,b), EM coefficient and magnetic force (Fig. 3a,b), voltage and instantaneous power (Fig. 5c,d) in the time response as the levitating-magnet moves through different positions between the coils, is indicated by the numbers 1-5. Since the magnet moves with high velocity during half a cycle through the top, bottom, and middle positions between the coils, where the EM coupling has local maxima, the output voltage and power in Fig. 5c,d have a dominant component with three times the input frequency, as provided by the discrete Fourier transform in Fig. 5e. Fig. 5f shows the initial conditions of displacement/velocity (null initial current) and the corresponding steady state to which the system evolves. These conditions must be high enough and properly synchronized with the input excitation ($\propto \cos(\omega t)$) such that the magnet can achieve the high frequency non-linear resonant state. While sweeping the frequency, after a steady state with the displacement amplitude $|\hat{\delta}|$, the initial conditions for a subsequent step should have a phase lag approx. as in: $\delta(0) = |\hat{\delta}| \cos(-\theta)$ and $\dot{\delta}(0) = -\omega|\hat{\delta}| \sin(-\theta)$, with $0 \leq \theta \leq \pi$, corresponding to the positive initial velocity semi-plane in Fig. 5f. As the input frequency decreases, the non-linear resonance region in Fig. 5f grows and the two steady-state amplitudes converge until combining.
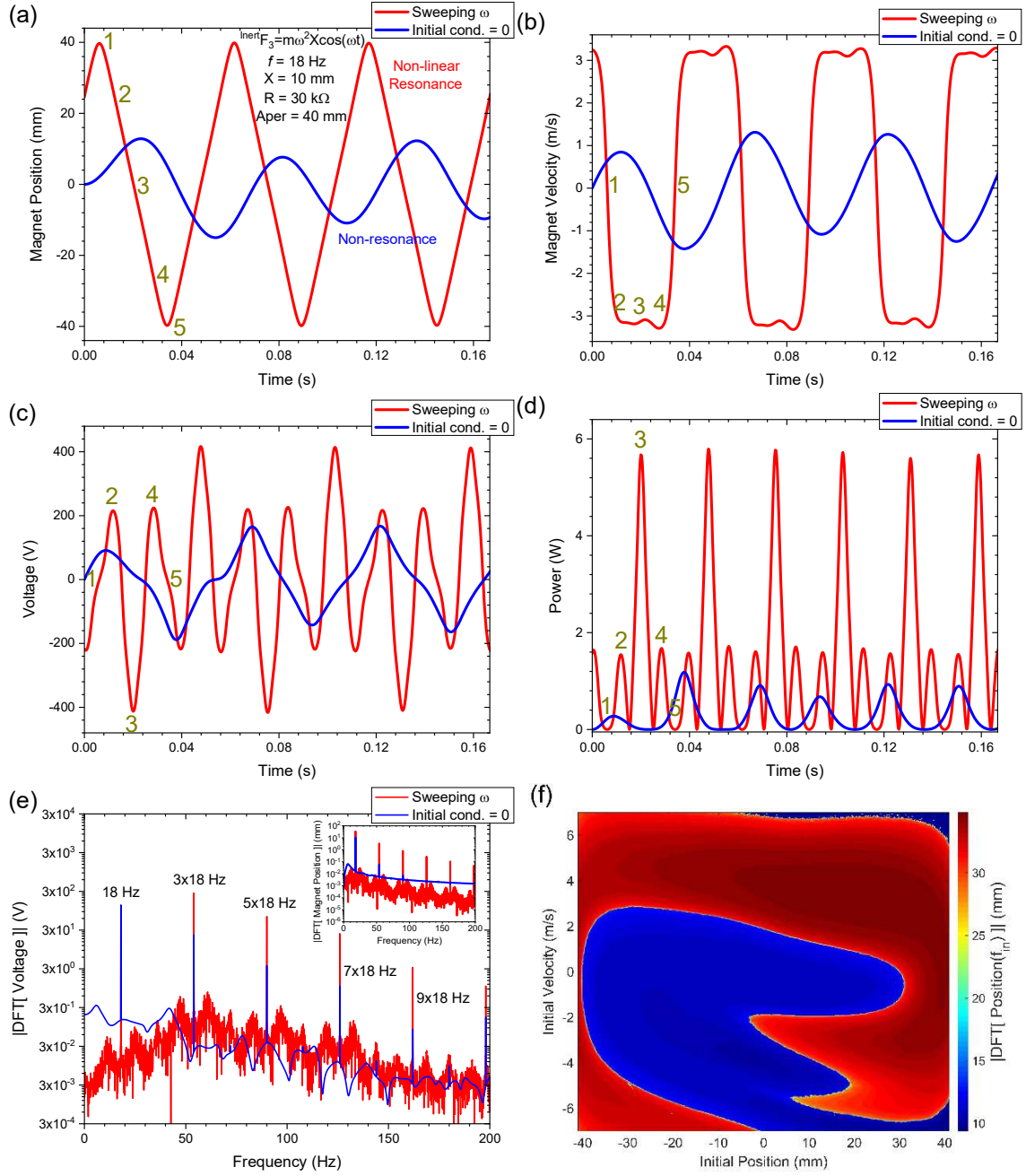
Fig. 5: Time response of the EMG (aperture of 40 mm) to a harmonic translational input with high amplitude $X = 10$ mm and frequency $f = 18$ Hz for an optimal load resistance of $R = 30$ kΩ with high (i.e. from sweeping the frequency) or null displacement/velocity initial conditions. (a) Position of the levitating-magnet; (b) Velocity of the levitating-magnet; (c) Voltage; (d) Instantaneous electrical power. 1-5 labels correspondent to those in the EM coupling and magnetic force in Fig. 3 are indicated; (e) Absolute value of the discrete Fourier transform for the voltage and magnet position (in the inset); (f) Amplitude of the displacement, in color scale, associated with the resonant or non-resonant steady state to which the system evolves as a function of the initial position and velocity conditions (for null initial current).

2.3 Experimental results and discussion. In order to validate the model of the transduction mechanism, the fundamental factors of magnetic force and EM coefficient, as a function of the position of the levitating-magnet, were experimentally measured. By superimposing the experimental results with the calculated curve in Fig. 3b, very good agreements were achieved.

The voltage output for different input frequencies and an amplitude of 3 mm, resistance of 200 kΩ, and aperture of 20 mm is provided in Fig. 6a. A non-linear resonance at an up-shifted frequency of ≈ 9.5 Hz is evidenced. Under these conditions, the time response has a large second harmonic component due to the

13

significant displacement amplitude and equilibrium position close to the center of the bottom coil (Fig. 3a). The frequency response for the same amplitude of 3 mm, aperture of 20 mm, and multiple load resistances was also obtained (Figs. 6 b-d). The voltage (Fig. 6b) and average power (Fig. 6c) follow a similar pattern to the calculated values in Figs. 4c,d, whose results have already been discussed in the model section. Since the excitation amplitude of displacement X was kept constant while the frequency ω was swept, the instantaneous power supplied by the generator system vary according to $\omega^3 X^2$, increasing very rapidly with the frequency, and resulting in output powers also increasing with the frequency. It is thus useful to normalize the power by the square of the acceleration $(\omega^2 X)^2$. Fig. 6d shows that the average power takes a maximum peak value of ≈ 15.5 mW/g^2 at a resonance frequency of 9 Hz for a matching resistance of the order of 10-100 kΩ, as predicted by Eq. (15c). In the linear regime, the power is maximal out of resonance conditions for a load equal to the internal resistance of the coil of ≈ 10 kΩ.
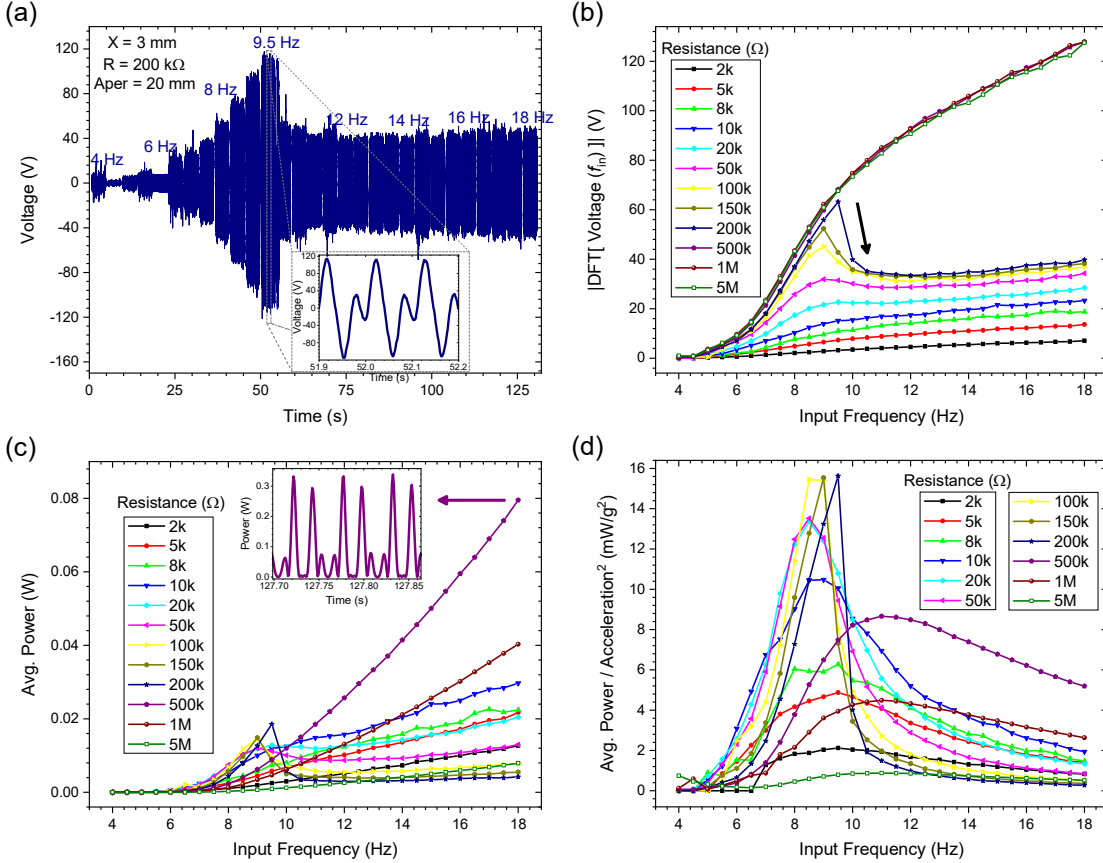

Fig. 6: (a) Experimentally measured voltage of the EMG (aperture of 20 mm) to a harmonic translation input with low amplitude $X = 3$ mm and a continuously increasing frequency (transition periods removed) for a load resistance of $R = 200$ kΩ. Frequency response of the (a) Voltage; (b) Average power; and (c) Average power normalized by the square of the input acceleration $(\omega^2 X)^2$ for different load resistances.

Figs. 7a,b show the peak voltage, peak current, and average power as a function of the load resistance for a large input displacement amplitude of 10 mm and frequency of 18 Hz, as well as for different apertures. For large enough resistances, the generation system is under non-linear resonance conditions where the outputs are enhanced and the displacement and velocity should be close to the maximum allowed values. The system with higher aperture values requires larger resistances to be able to maintain its non-linear resonance state up to 18 Hz, since its linear resonance frequency is significantly lower. Open-circuit voltage peaks up to ≈ 500 V, short-circuit current peaks up to 36.5 mA, and average powers of 1.5 W (with instantaneous power peaks up to 6 W) were obtained for matching loads of 10-30 kΩ. The average power in Fig. 7b exhibits two local maximum, a larger one under resonance for a larger matching load and a smaller one out of resonance for the internal resistance. For apertures lower or equal to10 mm, the two loads are very similar and the resonant state is maintained down to very low resistances. Even though the effective EM coupling might be lower for apertures lower than the maximum, the linear frequency of resonance is larger, which means that the system can reach the non-linear resonance state at 18 Hz for lower resistances R, closer to the internal resistance R_I, giving rise to larger effective velocity-to-power conversion ratios, $\langle P \rangle / \dot{\delta}^2 = R^{EM} \alpha(\delta)^2 / (R + R_I)^2$. Thus, the maximum output power was obtained for a

non-maximal aperture of 30 mm (Fig. 7b). Figs. 7c,d show the electrical output normalized by the input acceleration for a displacement amplitude of 10 mm and the frequency of resonance for each aperture. Open-circuit voltage peaks of ≈ 85 V/g, short-circuit current peaks of 2.9 mA/g and average powers of 26 mW/g^2 were measured for matching loads of 10-30 kΩ. Larger apertures are associated with larger effective EM constants ($^{EM}\alpha_0$), as is evidenced by Eqs. (15a-d), and thus to open-circuit voltages, except for the aperture of 10 mm, where the 2nd harmonic output is dominant. The short-circuit current has a more complex dependence of the type $^{EM}\alpha_0/(c + {}^{EM}\alpha_0^2/R_I)$, increasing and then decreasing with $^{EM}\alpha_0$. The maximal average power changes with $^{EM}\alpha_0^2/(c + {}^{EM}\alpha_0^2/R_I)$ and the matching load with $R_I + {}^{EM}\alpha_0^2/c$, thus increasing with the EM coupling.
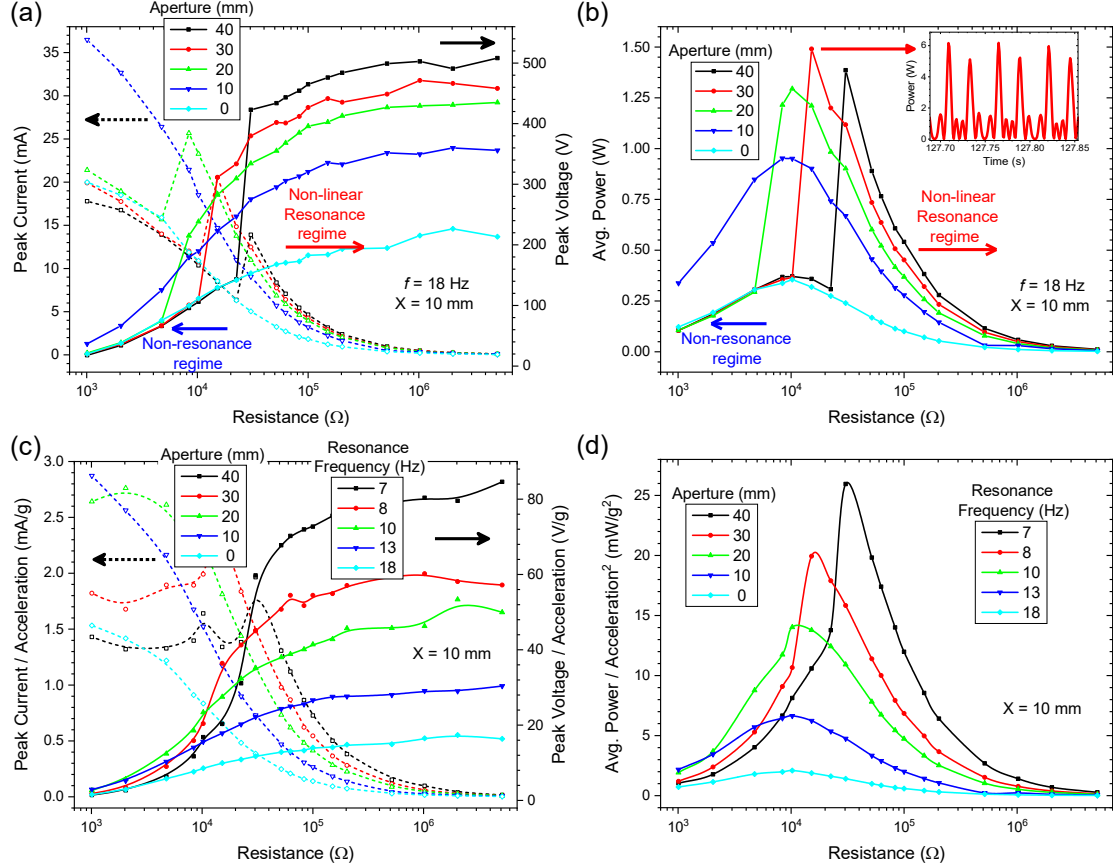

Fig. 7: (a) Peak voltage and current and (b) average power of the EMG for a large displacement amplitude of $X = 10$ mm and frequency of $f = 18$ Hz for different apertures as a function of the load resistance; (b) Peak voltage and current; and (c) Average power normalized by the input acceleration for a large $X = 10$ mm and linear frequency of resonance for each aperture as a function of the load resistance.

The maximum output average power, normalized by the square of the input acceleration measured for an optimal load resistance as a function of the input frequency and aperture for different input displacement amplitudes, is shown in Fig. 8. In general, maximum powers up to ≈ 26 mW/g^2 were obtained under resonance conditions, following the resonance frequency *vs* aperture relation as depicted in Fig. 3c. As the input amplitude increases, we observe a shift of the maximum power from larger frequencies and lower apertures to lower frequencies and larger apertures. At the lower amplitudes of excitation of 3 mm (Fig. 8a), the generator system can more easily attain higher displacements and velocities under resonance for the lower apertures of ≈ 10 mm, since these apertures are associated with low EM coupling in the equilibrium position, where the velocity is typically maximal, and thus Lorentz braking forces are low. This should be further exacerbated by the lower effective mechanical damping ratio (ζ_M) for the friction force in Eq. (13) associated with larger velocities. For medium amplitudes of 5 and 7 mm (Fig. 8b,c), the generator system is able to attain high displacements and velocities for lower resonance frequencies at larger apertures, which are also associated with larger average square of the EM coupling factors and, thus, to larger output powers. At the larger amplitudes of 10 mm (Fig. 8d), the displacements and velocities are very large and tend to saturate for the lower apertures, due to the lower upper limits imposed, resulting in higher output powers for the higher apertures. These results demonstrate the benefit of changing the

aperture of the EMG to maximize the output power as a function of the frequency and amplitude of the input signal (external mechanical excitation).
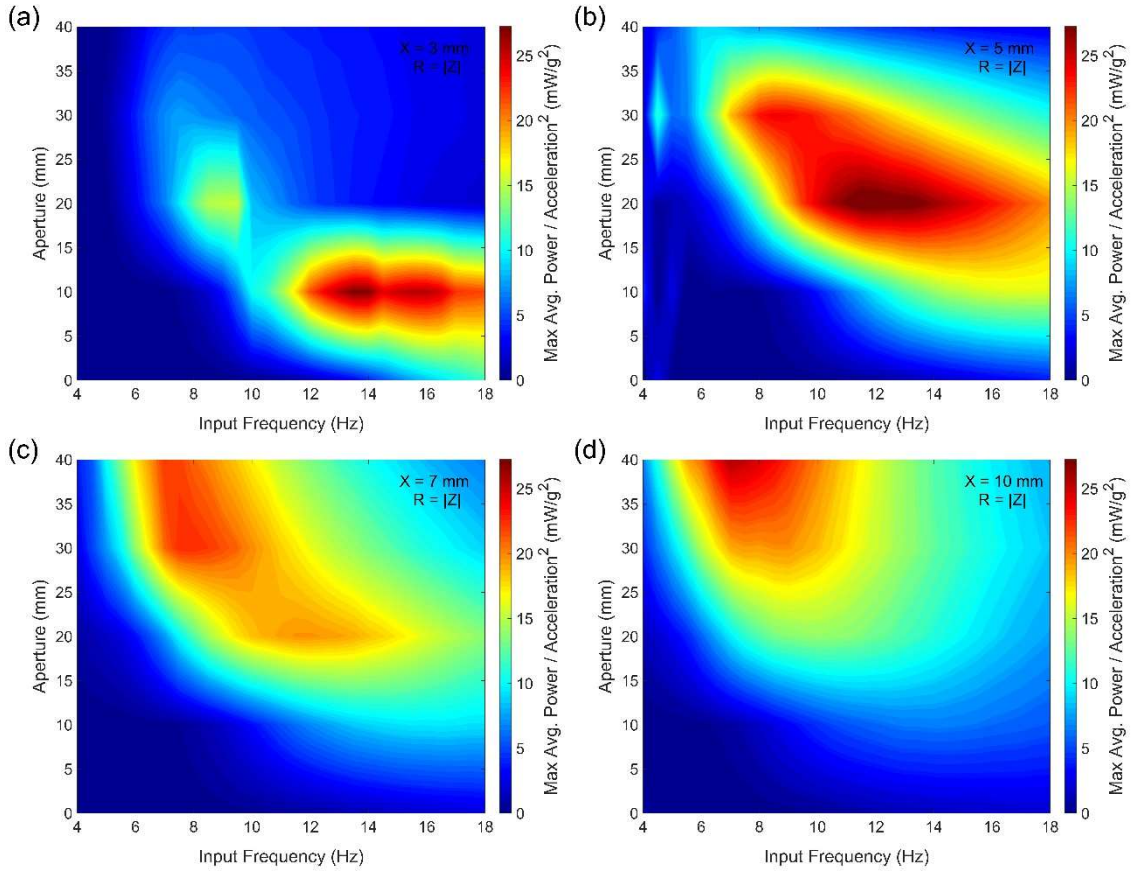

Fig. 8: Maximum output average power normalized by the square of the input acceleration $(\omega^2 X)^2$, in color scale, for an optimal load resistance as a function of the input frequency and aperture using input displacement amplitude X of (a) 3 mm; (b) 5 mm; (c) 7 mm and (d) 10 mm.

The total harvested power can be visualized in the scalar volume data plots in Fig. 9a,b, with isosurfaces of the maximum output average powers for an optimal load, represented as a function of the apertures, input displacement amplitudes, and frequencies. The experimentally obtained and calculated results (Fig. 9a,b) highlight the general increase of the power with the frequency and amplitude, as well as local maxima at the apertures for the linear frequency of resonance, for lower values of the amplitude, and for larger values of the amplitude at the highest aperture. The maximum output average power measured for corresponding optimal apertures and resistances, as a function of the displacement amplitude and frequency of the input excitation, are shown in Fig. 9c,e,g. The same results calculated using the model developed from first principles with a higher resolution on the amplitude, aperture, and resistance are depicted in Fig. 9d,f,h. The small differences between the experiment and simulation results should most likely be attributed to discrepancies between the geometric and EM parameters of the EMG, the form of the friction forces, and possibly small dangling oscillations of the levitating-magnet due to the magnetic torque. For large amplitudes and frequencies, the output power is shown to increase roughly with the acceleration $\omega^2 X$ up to a maximum of 1.5 W at 10 mm and 18 Hz (Fig. 9c,d). As evidenced by Fig. 9e,f, at the lower frequencies lower than 6 Hz, the generator system is in a non-resonant state. Larger electric powers can be harvested for the maximum aperture of 40 mm, since this is related to the lowest resonant frequency (ω_0) and largest EM coupling $(^{EM}\alpha_0)$ and, thus, referring to the linear solutions in Eq. (15), to larger displacements, velocities and currents. At higher frequencies, the generation system is in a resonant state. The maximum power will generally be achieved for lower amplitudes and lower apertures with resonance frequencies matching the input frequency. For larger frequencies and amplitudes, the displacement magnitude of the levitating-magnet is large under non-linear resonance conditions.
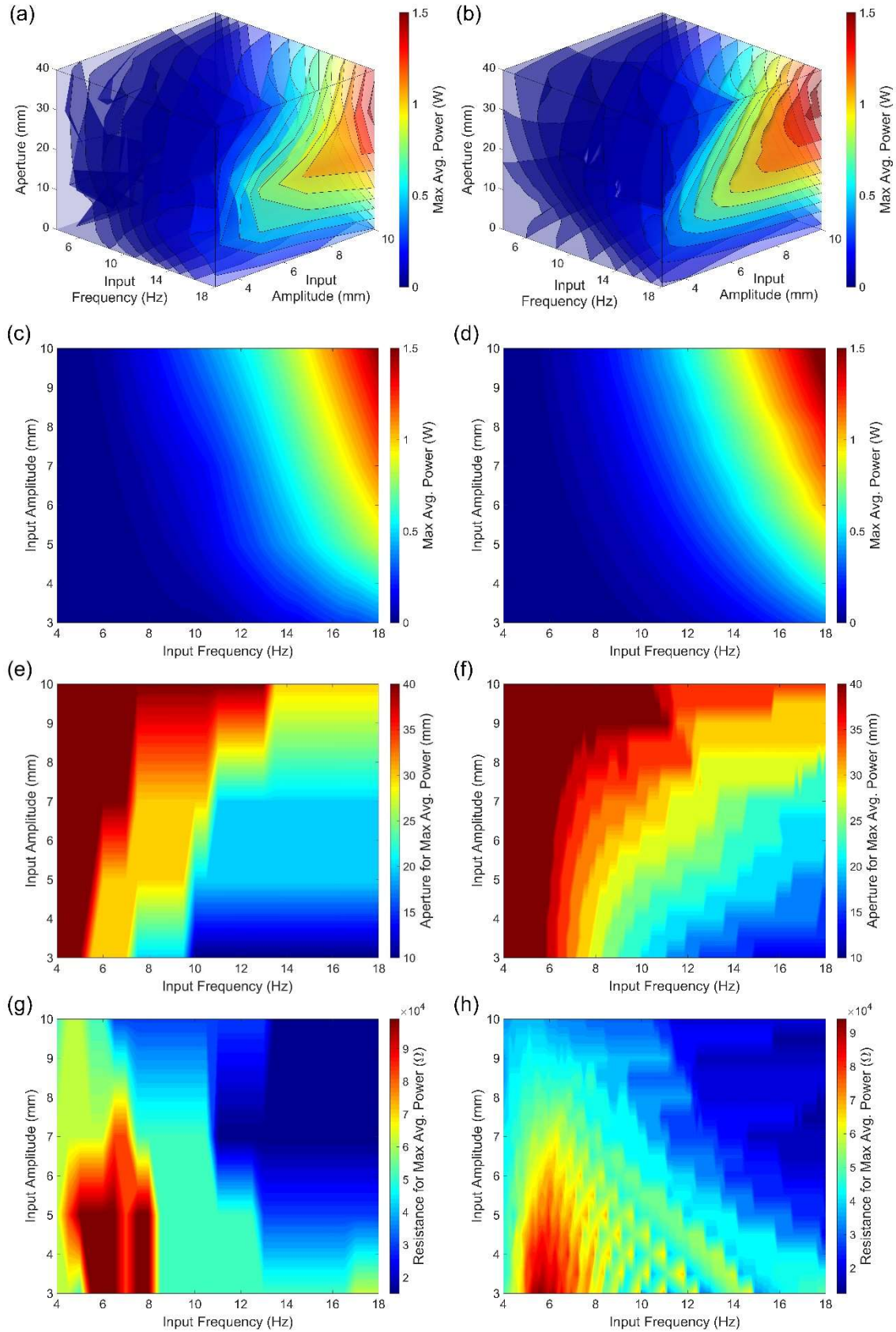
Fig. 9: (a,b) Isosurfaces of maximum output average power for an optimal load resistance as a function of the apertures, input displacement amplitudes, and frequencies; (c,d) Maximum output average power, in color scale, as a function of the amplitude and frequency of an input signal for a corresponding optimal (e,f) Aperture and (g,h) Resistance. (a,c,e,g) Experimental results; (b,d,f,h) Calculated results using the model derived from first principles.

The low average EM coupling and the upper limit imposed on the displacement for the lower apertures thus result in a shift of the maximum output powers to the larger apertures. The matching load resistance for maximum extracted power varies approx. between 15-100 kΩ and is significantly larger in the regions corresponding to the larger EM coupling and the linear resonance regime (Fig. 9g,h).

In order to validate the concept of the active self-adaptive electromagnetic energy harvester, we used a Monte Carlo method to analyze the output energy performance of the device with a random input excitation with a decreasing reciprocal probability distribution of displacement amplitudes and frequencies. The energy demand from the adaptive mechanism, namely the sensing, processing, and actuation systems, was considered. The total electrical energy extracted by a load during a time interval between t_1 and t_2 is:

$$E = \int_{t_1}^{t_2}[P(y(t),x(t),t) - P_-(\dot{y}(t),y(t),t)]\,dt, \tag{16}$$

where P is the instantaneous power received by the load, P_- are the power losses from the self-adaptive system, $y(t)$ are the time changing adaptive variables of aperture and load, and $x(t)$ are the input excitation variables of amplitude and frequency. The objective is, for given input parameters $x(t)$ in a time interval, to find the optimum corresponding control variables $y(t)$ that maximize the energy integral, as expressed by Eq. (16). If the integrand is continuously differentiable, a solution is achievable by solving the associated Euler-Lagrange equation.

Multiple case studies were carried out using different control algorithms. Sinusoidal excitations with random continuously changing amplitudes and frequencies, with a characteristic stability time (τ) over which they slowly change, were considered as depicted in Fig. 10a. The control algorithm measures the inputs and adapts the system in time steps of $\Delta t = t_2 - t_1$. If t_1 is the present time, the form of the input signal between t_1 and t_2 is not known *a priori* and can only be estimated from past sensor data. In the simplest scenario, the input signal used in the control algorithm can be assumed to be constant and equal to its value measured at present $x(t_1)$ (Fig. 10a). For simplicity, we assume the electrical load always corresponds to the optimal load for maximum power output and $y(t)$ represents the aperture. We considered time constant power losses associated with the sensors and processors: $P_{-,Control} = C$. The stepper motor that changes the aperture yield power losses of the form: $P_{-,Motor} = Fv$, where F is the force that it applies and v the speed of the changing aperture. The system changes the aperture beginning at the time t_1, with a constant positive or negative velocity v, until attaining a final value $y(t_1')$ at a time: $t_1' = t_1 + [y(t_1') - y(t_1)]/v$. With these considerations, the estimated energy gain in the $t_2 - t_1$ time interval has the form:

$$E_{Estimated} = \int_{t_1}^{t_1'} \langle P(y(t_1) + v.(t-t_1), x(t_1))\rangle\,dt + \int_{t_1'}^{t_2} \langle P(y(t_1'), x(t_1))\rangle dt - C.(t_2 - t_1)$$
$$- |Fv/v||y(t_1') - y(t_1)| \tag{17}$$

This gain can be computed in each interval for various achievable final apertures $y(t_1')$ (or equivalently, motor operation times $t_1' - t_1$) to find the corresponding optimal value that should maximize the energy harvested. The real energy gain for the actual input $x(t)$ can then be obtained as in Eq. (16).

Analyses were conducted considering the power consumption of a real hardware apparatus. The harvester was excited with random patterns with frequencies in the range of 4-18 Hz and amplitudes in the range of 3-10 mm, having a realistic decreasing $1/f$ reciprocal probability distribution as shown in the inset of Fig. 10a. The tested control algorithms included: (i) a reference measurement (Reference), where the generator operates with a constant aperture equal to 30 mm, corresponding to the aperture for the maximum measured power, and with no energy losses related to the adapting mechanism (i.e. effectively with no self-adaptation); (ii) A method (Max P. Chase) where the system periodically adapts the aperture to the input excitation to maximize the output electrical power, chasing the local power peak as in Fig. 9e,f; (iii) An algorithm (Optimal) that maximize the total energy gain from the self-adapting EMG by taking into account the power losses, achieved by maximizing Eq. (17). The results obtained for these different case studies as a function of time are represented in Fig. 10b, for a stability time of $\tau = 200$ s and a control time of $\Delta t = 40$ s. Overall, the Reference case achieved a long-term average power gain of 122 mJ/s, while the Max P. Chase method yielded 152 mJ/s and the Optimum algorithm a maximum value of 156 mJ/s. Therefore, the self-adaptation mechanism provided 28% energy gain in relation to the non-adaptive generator, as shown in the inset in Fig. 10b. The Max P. Chase algorithm resulted in the largest variations of the aperture and consequently significant energy losses (Fig. 10b), although the energy gain was still superior to that of the

reference configuration. Fig. 10c depicts the long-term energy gain with the reference configuration as a function of the stability time of the input signal. If this time is too small, the self-adapting mechanism is not fast enough and, thus, the potential extractable energy gains from changing the configuration during these small time intervals are not enough to compensate the power losses. This results in potentially negative and null energy gains from the Max P. Chase and Optimal algorithms, respectively. As the stability time increases, both ensure positive gains up to a maximum of $\approx$ 30%. For lower control/sensing times, such as $\Delta t = \tau/2$, the adaptive system will follow the time-changing input frequencies and amplitudes less closely (as in Fig. 10a), and thus, lower energy gains for large stability times will be observed. On the other hand, due to the larger integrating times in Eq. (17), the algorithm more readily detects possible energy gains from changing the aperture by a fixed amount for lower values of the stability time. We should note that the values of the power losses influence these results, especially those associated with the motor, since the ones related to the sensor and controllers are comparatively insignificant. Large losses from the motor result in the Max P. Chase algorithm generally yielding energy losses and the Optimum algorithm tending towards the Reference case. Low losses result in the Max P. Chase and Optimum algorithms yielding maximum energy gains, which in the limit can increase up to $\approx$ 35%, as shown in Fig. 10c. This value drops for small stability times due to the finite velocity of changing the aperture. Overall, better energy gains could be expected if it weren't for the relatively low Q factor of the system ($\approx$ 1–5), resulting in small and wide resonance power peaks and, thus, small energy returns from changing the aperture.

3. Conclusions

This study analyzes the concept of self-adapting instrumented levitating electromagnetic generator. A model based on first principles was developed and experimentally validated. The ability of the self-adapting generator to provide significant power gains were both theoretically and experimentally demonstrated. An initial condition-dependent non-linear resonant behavior up to large frequencies was observed. Although this generator exhibits a volume of 140.7 cm^3, maximum open-circuit resonant voltage peak values up to $\approx$ 500 V, short-circuit current peaks of 36.5 mA and average powers of 1.5 W (with instantaneous power peaks up to 6 W) were achieved for matching loads of 10-30 kΩ under translational excitations with displacement amplitudes of 3-10 mm and frequencies of 4-18 Hz. The maximum power output was achieved under different conditions of input amplitudes and frequencies for corresponding controlled optimal loads and distances between fixed magnets. A Monte Carlo method for different case studies showed the ability of the self-adaptation mechanism to provide energy gains that can surpass 30%. Results prove the potential of self-adaptability to significantly enhance the efficiency of electromagnetic generators designed to convert the ubiquitous mechanical energy into electric one. Despite the impressive findings here presented, future technological breakthroughs will most likely imply to address the following issues:

(i) Frequency and amplitude of mechanical excitations must be accurately predicted to ensure optimized decision making regarding switching the adaptive mechanisms on/off. Many applications experience time-varying mechanical excitations patterns, as occur in mechanical sources driving renewable energy systems (ocean and wind energy, etc.) [22, 25] and human-induced motion [56, 57]. The response of the generator to more general input excitations, with broad frequency spectrums and movements, must be studied in detail, including changes of orientation (i.e. with inertial forces containing centrifugal and gravitational components, as in Eq. (4b)), irregularities and white noise. This problem is highly complex due to the non-linear nature of the device, which require very large computational and experimental costs, although in general the system would still be expected to aim at tuning its resonance frequency to the higher power components of the input spectrum (i.e. higher frequencies and amplitudes). Therefore, predictive algorithms are mandatory, including autonomous machine learning of external excitations and intelligent decision making (to optimize the aperture dynamics, etc.), to ensure the high efficiency of the self-adaptive mechanisms for universal applications. Regardless, adaptation to fast randomly changing excitations might still prove unfeasible due to poor decision making and slow actuation times [58].

(ii) Innovative magnetic levitation architectures, comprising also innovative self-adaptive instrumentation, must be designed to increase energy efficiency. Particular attention is required for generators operating at a very low frequency (lower than 2 Hz). Forms of decreasing the resonance frequency of the generator could involve increasing the mass of the levitating-stack, increasing the distance between or decreasing the size and magnetization of the fixed magnets. Advanced power management methods for impedance matching and energy transfer maximization are also desirable. More sophisticated designs can also make use of the output voltage from the coils to determine the characteristics of the input excitations and operate in a closed-loop control approach.

(iii) Miniaturization of these instrumented generators, including the actuation components, is demanded to power small-scale devices. Downscaling may be hard to achieve using conventional machining technology. Therefore, advanced manufacturing methods will most likely be essential.

(iv) Implementation of self-adaptive mechanisms to other electromagnetic generators. Considering the huge amount of electromagnetic generation architectures [24, 59], customized self-adaptability may be desirable. Instrumented generators must be designed to avoid additional power losses for smaller apertures and/or when the positional-controlled non-levitating magnet experiences significant magnetic forces.

(v) Integration of instrumentation for self-adaptability into hybrid generators, such as hybrid electromagnetic-piezoelectric and electromagnetic-triboelectric generators [35, 60, 61].

Results here presented, as well as the future research directions proposed, are strong indicators that self-adaptability of energy harvesters is a new research area that may conduct to great impacts in the coming years.
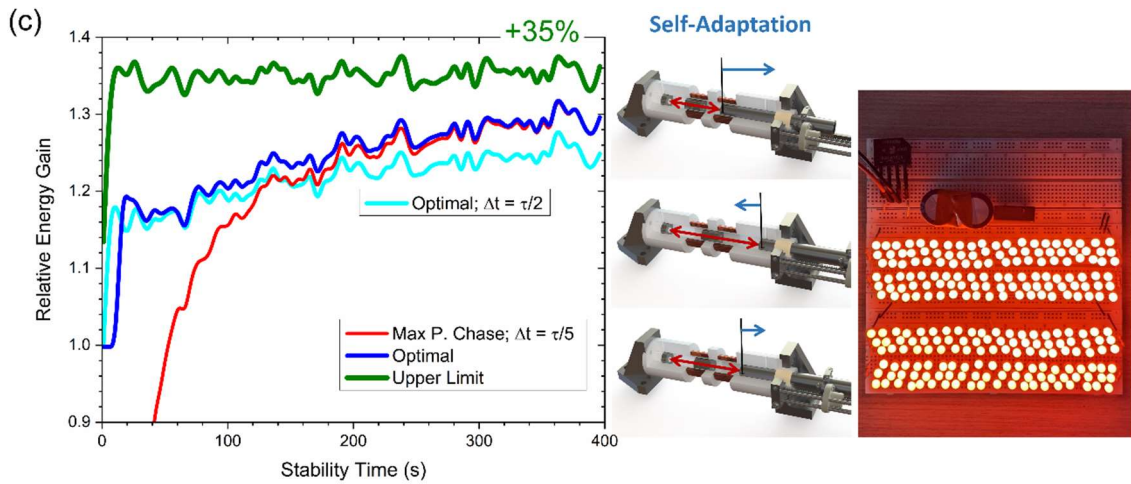

Fig. 10: (a) Input frequency of the time changing sinusoidal excitation used in the Monte Carlo self-adaptive energy gain model. The estimated form of the input signal, based on the periodic information obtained from the sensor units, is represented. The inset shows the decreasing $1/f$ reciprocal probability distribution histogram of the input frequencies (similar to the one used for the input amplitudes); (b) Energy generated as a function of time for a reference configuration (Reference), with no self-adaptation mechanism, and following two adaptation algorithms: chasing the maximum electrical power output (Max P. Chase), with no regard to the power losses, and optimizing the total energy gain (Optimal). The corresponding adaptive variation of the aperture of the EMG is also presented as a function of time; (c) Total long-term energy gain in relation to the reference configuration as a function of the stability time (τ) of the sinusoidal input signal for two control times (Δt). The upper limit of the energy gain, which can potentially be obtained in case the energy losses associated with the self-adaptation mechanism were null, is represented. A photo-realistic representation of the instrumented self-adapting harvester under operation (with the actuation and sensing structures partially omitted) and energy generator powering 240 LEDs by using an exciting of 10 mm amplitude and 18 Hz frequency under optimal aperture, is also shown.

4. Methods

4.1 Numerical calculations. The dynamic differential Eq. (14) was solved numerically using Runge-Kutta methods through Matlab (v. 9.4, Mathworks) solver ode45 (low frequency approximation) and solver

ode15s in a time span of $n2\pi/\omega$, with $n \in \mathbb{N}$ the number of cycles. The magnetic forces and EM coefficients as a function of the position were previously calculated using Eqs. (10) and (7b,8b) and the integral function and saved in lookup tables. These parameters were spline interpolated for faster numerical performance, with the additional advantage of the force term exploding to infinity at negative distance between magnets (representing elastic collisions), thus introducing a natural constrain that keeps the levitating-magnet from escaping the container. The loops of a closely packed coil were described by indexes j, l and k with: $j = l + (k-1)N_L$, radius ${}^{lj}\rho = {}^{I}\rho_L + (\sqrt{3}/2)(k-1)\Phi$ and axial position ${}^{lj}z = {}^{I}z_L + \text{sign}({}^{I}z_L)[(l-1)\Phi + (1/4)(1 + (-1)^k)\Phi]$, where k is the radial and l the axial index, ${}^{I}\rho_L$ the inner radius and ${}^{I}z_L$ the position of the first loop of the coil in relation to the center of the container, N_L the total number of loops along the z direction and N_P the total number of loops along the ρ direction. The inner resistance can be estimated by: $R_I = \rho_{resist}.\text{Length}/\text{Area}$, with $\text{Length} = 2\pi N_L N_P({}^{I}\rho_L + (N_P - 1)(\sqrt{3}/4)\Phi)$ and $\text{Area} = \pi(\Phi/2)^2$, where ρ_{resist} is the electrical resistivity of the conductor material.

4.2 Instrumentation of the adaptive harvester. The excitation driving the harvester was monitored by an ultra-low power accelerometer (BMA400, Bosch Sensortec), which requires 52.2 μW of power consumption. A step motor (DM0620, Faulhaber Minimotor) of 0.25 mNm and ≈ 0.48 W of nominal power consumption ($|Fv| = 0.48$ W) was used as the actuation system to perform the optimal positioning of the top non-levitating magnet. The average velocity of the changing aperture was experimentally monitored as $|v| \approx 5$ mm/s. The overall system was controlled by an ultra-low power microcontroller (MSP430, Texas Instruments) demanding 66 μW to perform processing operations ($C = 118.2$ μW), including monitoring of the mechanical excitations and command operations using the optimal apertures of the container. The ultrasonic sensor (microsonic nano-15/CU) was only used for model validation purpose.

4.3 Energy gain model. The harvester was excited with random patterns with frequencies in the range of 4-18 Hz and amplitudes in the range of 3-10 mm, having a realistic decreasing reciprocal probability distribution between a and b ($f(y; a, b) = 1/(y \ln(b/a))$) associated with the random variable: $Y = a.\exp(X.\ln(b/a))$, with X a uniformly distributed random number between 0 and 1. The values of the output average power in Eq. (17) as a function of the frequency, amplitude, resistance and aperture were interpolated from the experimental results. The dependence of the power with the initial conditions was not considered but assumed to affect the different case studies in approx. the same way. The stability time was set to $\tau = 1\text{-}400$ s and the control time to $\Delta t = \tau/n, n \in \mathbb{N}$, and results were obtained over a long time span of $\tau.10^4$ s.

4.4 Mechanical excitation apparatus. Digital I/O channels from a DSP board (DS1104 from dSPACE) were integrated with Matlab (v. 9.4, Mathworks) and Simulink (v. 9.1, Mathworks) using Real-Time Workshop (v. 5.6, Mathworks) and the Real-Time Interface (v. 7.12, dSPACE). A software application was developed in ControlDesk (v. 7.0, dSPACE) to interact with a real-time system, which was used to control the mechanical excitation system, a slider-crank mechanism actuated by an AC Motor (W21 90S, WEG) and an AC Inverter Drive (EFC3610-1K50, Bosch).

4.5 Features of the adaptive generator. To maximize the harvester performance, the container was manufactured using PTFE, as it ensures low friction coefficient. Its architecture was designed to ensure a 1.25 mm tight-fit container-magnet interface. Appropriate materials with negligible magnetic permeability and electrical conductivity properties were carefully selected; bushings were incorporated whenever the assembly required rotating, oscillating and linear movements. The cylindrical dimensions of the manufactured container are $\Phi40\times112$ mm. The actuation and sensing mechanisms were positioned at different extremities of the container. Ring magnets were preferred, allowing the inertial guiding rod (which is coupled to the levitating-magnet) to pass through the center of the hard-magnetic elements; the ultrasonic sensor is concentric with the harvester shaft and fixed to the adaptive structure. The rotational step motor motion is converted into linear magnet motion through a trapezoidal spindle, nut and two rods - the nut is screwed to a hollowed tube, which in turn is rigidly coupled to the adaptively positioned magnet.

4.6 Experimental testing. The magnetic force between the bottom fixed magnet and the levitating-magnet was tested as a function of the distance between them by coupling different masses (from 60 g to 3.25 kg) to the latter magnet and measuring its corresponding equilibrium position inside the container under the gravitational field. Values of the EM coefficient and resonance frequency were measured by fitting the voltage frequency response of the EMG, operating under low amplitude harmonic input conditions, to the linear voltage expression in Eq. (15b) for different apertures, as represented in Figs. 3a,c. The time response of the voltage of the system was measured while applying a sinusoidal axial translation input with constant

displacement amplitude of 3, 5, 7 and 10 mm and sweeping the frequency from 4 to 18 Hz. Multiple load resistances from 1 kΩ to 5 MΩ were tested as well as different apertures of 0, 10, 20, 30 and 40 mm.

CRediT Authorship contribution statement
Pedro Carneiro: Methodology, Software, Investigation, Validation, Writing- Original draft. **Joao Vidal:** Methodology, Software, Investigation, Formal analysis, Data curation, Writing- Original draft. **Pedro Rolo**: Visualization, Investigation, Writing – Review & Editing. **Inês Peres:** Formal analysis, Investigation, Writing – Review & Editing. **Jorge Ferreira:** Formal Analysis, Writing – Review & Editing. **Andrei Kholkin:** Funding acquisition, Project Administration, Writing- Reviewing and Editing, **Marco Soares dos Santos:** Funding acquisition, Resources, Conceptualization, Project Administration, Supervision, Formal Analysis, Writing – Review & Editing.
Pedro Carneiro and **Joao Vidal** contributed equally to this work.

Competing interests
The authors declare no competing interests.

References

[1] H. Lv, Z. Yang, B. Liu, G. Wu, Z. Lou, B. Fei, R. Wu, "A flexible electromagnetic wave-electricity harvester", *Nat. Commun.*, **12**(1), 834, (2021). http://doi.org/10.1038/s41467-021-21103-9

[2] K. Calautit, D. S. N. M. Nasir, B. R. Hughes, "Low power energy harvesting systems: State of the art and future challenges", *Renew. Sustain. Energy Rev.*, **147** 111230, (2021). http://doi.org/10.1016/j.rser.2021.111230

[3] C. Zhang, J. Chen, W. Xuan, S. Huang, B. You, W. Li, L. Sun, H. Jin, X. Wang, S. Dong, J. Luo, A. J. Flewitt, Z. L. Wang, "Conjunction of triboelectric nanogenerator with induction coils as wireless power sources and self-powered wireless sensors", *Nat. Commun.*, **11**(1), 58, (2020). http://doi.org/10.1038/s41467-019-13653-w

[4] J. Kim, M. Kim, M.-S. Lee, K. Kim, S. Ji, Y.-T. Kim, J. Park, K. Na, K.-H. Bae, H. Kyun Kim, F. Bien, C. Young Lee, J.-U. Park, "Wearable smart sensor systems integrated on soft contact lenses for wireless ocular diagnostics", *Nat. Commun.*, **8**(1), 14997, (2017). http://doi.org/10.1038/ncomms14997

[5] R. Sharma, R. Mishra, T. Ngo, Y.-X. Guo, S. Fukami, H. Sato, H. Ohno, H. Yang, "Electrically connected spin-torque oscillators array for 2.4 GHz WiFi band transmission and energy harvesting", *Nat. Commun.*, **12**(1), 2924, (2021). http://doi.org/10.1038/s41467-021-23181-1

[6] J. Dunn, L. Kidzinski, R. Runge, D. Witt, J. L. Hicks, S. M. Schüssler-Fiorenza Rose, X. Li, A. Bahmani, S. L. Delp, T. Hastie, M. P. Snyder, "Wearable sensors enable personalized predictions of clinical laboratory measurements", *Nat. Med.*, **27**(6), 1105, (2021). http://doi.org/10.1038/s41591-021-01339-0

[7] M. P. Soares Dos Santos, R. Bernardo, L. Henriques, A. Ramos, J. A. F. Ferreira, E. P. Furlani, A. Torres Marques, J. A. O. Simões, "Towards an effective sensing technology to monitor micro-scale interface loosening of bioelectronic implants", *Sci. Rep.*, **11**(1), 3449, (2021). http://doi.org/10.1038/s41598-021-82589-3

[8] J. Ausra, S. J. Munger, A. Azami, A. Burton, R. Peralta, J. E. Miller, P. Gutruf, "Wireless battery free fully implantable multimodal recording and neuromodulation tools for songbirds", *Nat. Commun.*, **12**(1), 1968, (2021). http://doi.org/10.1038/s41467-021-22138-8

[9] C. Y. Kim, M. J. Ku, R. Qazi, H. J. Nam, J. W. Park, K. S. Nam, S. Oh, I. Kang, J.-H. Jang, W. Y. Kim, J.-H. Kim, J.-W. Jeong, "Soft subdermal implant capable of wireless battery charging and programmable

controls for applications in optogenetics", *Nat. Commun.*, **12**(1), 535, (2021). http://doi.org/10.1038/s41467-020-20803-y

[10] M. P. Soares dos Santos, J. Coutinho, A. Marote, B. Sousa, A. Ramos, J. A. F. Ferreira, R. Bernardo, A. Rodrigues, A. T. Marques, O. A. B. d. Cruz e Silva, E. P. Furlani, J. A. O. Simões, S. I. Vieira, "Capacitive technologies for highly controlled and personalized electrical stimulation by implantable biomedical systems", *Sci. Rep.*, **9**(1), 5001, (2019). http://doi.org/10.1038/s41598-019-41540-3

[11] H. Alemzadeh, R. K. Iyer, Z. Kalbarczyk, J. Raman, "Analysis of Safety-Critical Computer Failures in Medical Devices", *IEEE Secur. & Priv.*, **11**(4), 14, (2013). http://doi.org/10.1109/MSP.2013.49

[12] M. P. Soares dos Santos, J. A. F. Ferreira, A. Ramos, J. A. O. Simões, "Active orthopaedic implants: Towards optimality", *J. Franklin Inst.*, **352**(3), 813, (2015). http://doi.org/10.1016/j.jfranklin.2014.11.005

[13] J. Yu, G. Gao, J. Huang, X. Yang, J. Han, H. Zhang, Y. Chen, C. Zhao, Q. Sun, Z. L. Wang, "Contact-electrification-activated artificial afferents at femtojoule energy", *Nat. Commun.*, **12**(1), 1581, (2021). http://doi.org/10.1038/s41467-021-21890-1

[14] X. Liu, M. Zhang, A. G. Richardson, T. H. Lucas, J. V. d. Spiegel, "Design of a Closed-Loop, Bidirectional Brain Machine Interface System With Energy Efficient Neural Feature Extraction and PID Control", *IEEE Trans. Biomed. Circuits Syst.*, **11**(4), 729, (2017). http://doi.org/10.1109/TBCAS.2016.2622738

[15] U.S. Energy Information Administration, International Energy Outlook 2021 - with Projections to 2050, 2021.

[16] European Comission. Energy roadmap 2050. European Union; 2012.

[17] International Renewable Energy Agency (IRENA). Global Energy Transformation – a Roadmap to 2050, 2018.

[18] X. Peng, Z. Liu, D. Jiang, "A review of multiphase energy conversion in wind power generation", *Renew. Sustain. Energy Rev.*, **147** 111172, (2021). http://doi.org/10.1016/j.rser.2021.111172

[19] D. Kraemer, B. Poudel, H.-P. Feng, J. C. Caylor, B. Yu, X. Yan, Y. Ma, X. Wang, D. Wang, A. Muto, K. McEnaney, M. Chiesa, Z. Ren, G. Chen, "High-performance flat-panel solar thermoelectric generators with high thermal concentration", *Nat. Mater.*, **10**(7), 532, (2011). http://doi.org/10.1038/nmat3013

[20] J. P. G. Tarelho, M. P. Soares dos Santos, J. A. F. Ferreira, A. Ramos, S. Kopyl, S. O. Kim, S. Hong, A. Kholkin, "Graphene-based materials and structures for energy harvesting with fluids – A review", *Mater. Today*, **21**(10), 1019, (2018). http://doi.org/10.1016/j.mattod.2018.06.004

[21] J. Yin, A. Molini, A. Porporato, "Impacts of solar intermittency on future photovoltaic reliability", *Nat. Commun.*, **11**(1), 4781, (2020). http://doi.org/10.1038/s41467-020-18602-6

[22] B. Barnier, A. Domina, S. Gulev, J.-M. Molines, T. Maitre, T. Penduff, J. Le Sommer, P. Brasseur, L. Brodeau, P. Colombo, "Modelling the impact of flow-driven turbine power plants on great wind-driven ocean currents and the assessment of their energy potential", *Nat. Energy*, **5**(3), 240, (2020). http://doi.org/10.1038/s41560-020-0580-2

[23] D. Elliott, "A balancing act for renewables", *Nat. Energy*, **1**(1), 15003, (2016). http://doi.org/10.1038/nenergy.2015.3

[24] P. Carneiro, M. P. Soares dos Santos, A. Rodrigues, J. A. F. Ferreira, J. A. O. Simões, A. T. Marques, A. L. Kholkin, "Electromagnetic energy harvesting using magnetic levitation architectures: A review", *Appl. Energy*, **260** 114191, (2020). http://doi.org/10.1016/j.apenergy.2019.114191

[25] Y. Zhang, Y. Zhao, W. Sun, J. Li, "Ocean wave energy converters: Technical principle, device realization, and performance evaluation", *Renew. Sust. Energ. Rev.*, **141** 110764, (2021). http://doi.org/10.1016/j.rser.2021.110764

[26] W. Gao, R. Brennan, Y. Hu, M. Wuttig, G. Yuan, E. Quandt, S. Ren, "Energy transduction ferroic materials", *Mater. Today*, **21**(7), 771, (2018). http://doi.org/10.1016/j.mattod.2018.01.032

[27] J. V. Vidal, A. V. Turutin, I. V. Kubasov, A. M. Kislyuk, D. A. Kiselev, M. D. Malinkovich, Y. N. Parkhomenko, S. P. Kobeleva, N. A. Sobolev, A. L. Kholkin, "Dual vibration and magnetic energy harvesting with bidomain LiNbO3 based composite", *IEEE Trans. Ultrason. Ferroelectr. Freq. Control*, (2020). http://doi.org/10.1109/tuffc.2020.2967842

[28] M. P. Soares dos Santos, J. A. F. Ferreira, J. A. O. Simões, R. Pascoal, J. Torrão, X. Xue, E. P. Furlani, "Magnetic levitation-based electromagnetic energy harvesting: a semi-analytical non-linear model for energy transduction", *Sci. Rep.*, **6** 18579, (2016). http://doi.org/10.1038/srep18579

[29] Q. Zheng, B. Shi, Z. Li, Z. L. Wang, "Recent Progress on Piezoelectric and Triboelectric Energy Harvesters in Biomedical Systems", *Adv. Sci.*, **4**(7), 1700029, (2017). http://doi.org/10.1002/advs.201700029

[30] R. L. Harne, M. E. Schoemaker, B. E. Dussault, K. W. Wang, "Wave heave energy conversion using modular multistability", *Appl. Energy*, **130** 148, (2014). http://doi.org/10.1016/j.apenergy.2014.05.038

[31] M. P. Soares dos Santos, J. A. F. Ferreira, A. Ramos, J. A. O. Simões, R. Morais, N. M. Silva, P. M. Santos, M. J. C. S. Reis, T. Oliveira, "Instrumented hip implants: Electric supply systems", *J. Biomech.*, **46**(15), 2561, (2013). http://doi.org/10.1016/j.jbiomech.2013.08.002

[32] H. Wang, L. Xu, Y. Bai, Z. L. Wang, "Pumping up the charge density of a triboelectric nanogenerator by charge-shuttling", *Nat. Commun.*, **11**(1), 4203, (2020). http://doi.org/10.1038/s41467-020-17891-1

[33] G. Aldawood, H. T. Nguyen, H. Bardaweel, "High power density spring-assisted nonlinear electromagnetic vibration energy harvester for low base-accelerations", *Appl. Energy*, **253** 113546, (2019). http://doi.org/10.1016/j.apenergy.2019.113546

[34] R. M. Toyabur, M. Salauddin, H. Cho, J. Y. Park, "A multimodal hybrid energy harvester based on piezoelectric-electromagnetic mechanisms for low-frequency ambient vibrations", *Energy Convers. Manag.*, **168** 454, (2018). http://doi.org/10.1016/j.enconman.2018.05.018

[35] J. He, T. Wen, S. Qian, Z. Zhang, Z. Tian, J. Zhu, J. Mu, X. Hou, W. Geng, J. Cho, J. Han, X. Chou, C. Xue, "Triboelectric-piezoelectric-electromagnetic hybrid nanogenerator for high-efficient vibration energy harvesting and self-powered wireless monitoring system", *Nano Energy*, **43** 326, (2018). http://doi.org/10.1016/j.nanoen.2017.11.039

[36] Y. Hu, J. Yang, S. Niu, W. Wu, Z. L. Wang, "Hybridizing Triboelectrification and Electromagnetic Induction Effects for High-Efficient Mechanical Energy Harvesting", *ACS nano*, **8**(7), 7442, (2014). http://doi.org/10.1021/nn502684f

[37] C. M. Saravia, "On the electromechanical coupling in electromagnetic vibration energy harvesters", *Mech. Syst. Signal Process.*, **136** 106027, (2020). http://doi.org/10.1016/j.ymssp.2019.03.026

[38] C. M. Saravia, "A formulation for modeling levitation based vibration energy harvesters undergoing finite motion", *Mech. Syst. Signal Process.*, **117** 862, (2019). http://doi.org/10.1016/j.ymssp.2018.08.023

[39] J. D. Jackson, "Classical Electrodynamics (3rd ed.)", New York: John Wiley & Sons., 1999.

[40] E. P. Furlani, "Permanent Magnet and Electromechanical Devices: Materials, Analysis, and Applications", Academic Press, 2001. http://doi.org/10.1016/B978-012269951-1/50001-2

[41] A. Zangwill, "Modern Electrodynamics", Cambridge University Press; 1st edition, 2012.

[42] P. Constantinou, P. H. Mellor, P. D. Wilcox, "A Magnetically Sprung Generator for Energy Harvesting Applications", *IEEE ASME Trans. Mechatron.*, **17**(3), 415, (2012). http://doi.org/10.1109/TMECH.2012.2188834

[43] S. Palagummi, F. G. Yuan, "An optimal design of a mono-stable vertical diamagnetic levitation based electromagnetic vibration energy harvester", *J. Sound Vib.*, **342** 330, (2015). http://doi.org/10.1016/j.jsv.2014.12.034

[44] G. Akoun, J. Yonnet, "3D analytical calculation of the forces exerted between two cuboidal magnets", *IEEE Trans. Magn.*, **20**(5), 1962, (1984). http://doi.org/10.1109/TMAG.1984.1063554

[45] B. P. Mann, B. A. Owens, "Investigations of a nonlinear energy harvester with a bistable potential well", *J. Sound Vib.*, **329**(9), 1215, (2010). http://doi.org/10.1016/j.jsv.2009.11.034

[46] W. Muller, "Comparison of different methods of force calculation", *IEEE Trans. Magn.*, **26**(2), 1058, (1990). http://doi.org/10.1109/20.106503

[47] T. Tarnhuvud, K. Reichert, "Accuracy problems of force and torque calculation in FE-systems", *IEEE Trans. Magn.*, **24**(1), 443, (1988). http://doi.org/10.1109/20.43952

[48] R. Ravaud, G. Lemarquand, S. Babic, V. Lemarquand, C. Akyel, "Cylindrical Magnets and Coils: Fields, Forces, and Inductances", *IEEE Trans. Magn.*, **46**(9), 3585, (2010). http://doi.org/10.1109/TMAG.2010.2049026

[49] M. L. Morgado, L. F. Morgado, N. Silva, R. Morais, "Mathematical modelling of cylindrical electromagnetic vibration energy harvesters", *Int. J. Comput. Math.*, **92**(1), 101, (2015). http://doi.org/10.1080/00207160.2014.884715

[50] A. G. Avila Bernal, L. E. Linares García, "The modelling of an electromagnetic energy harvesting architecture", *Appl. Math. Model.*, **36**(10), 4728, (2012). http://doi.org/10.1016/j.apm.2011.12.007

[51] D. F. Berdy, D. J. Valentino, D. Peroulis, "Design and optimization of a magnetically sprung block magnet vibration energy harvester", *Sens. Actuators A-Phys.*, **218** 69, (2014). http://doi.org/10.1016/j.sna.2014.06.011

[52] B. P. Mann, N. D. Sims, "Energy harvesting from the nonlinear oscillations of magnetic levitation", *J. Sound Vib.*, **319**(1), 515, (2009). http://doi.org/10.1016/j.jsv.2008.06.011

[53] C. M. Saravia, J. M. Ramírez, C. D. Gatti, "A hybrid numerical-analytical approach for modeling levitation based vibration energy harvesters", *Sens. Actuators A-Phys.*, **257** 20, (2017). http://doi.org/10.1016/j.sna.2017.01.023

[54] N. G. Stephen, "On energy harvesting from ambient vibration", *J. Sound Vib.*, **293**(1), 409, (2006). http://doi.org/10.1016/j.jsv.2005.10.003

[55] L. Liu, F. G. Yuan, "Diamagnetic levitation for nonlinear vibration energy harvesting: Theoretical modeling and analysis", *J. Sound Vib.*, **332**(2), 455, (2013). http://doi.org/10.1016/j.jsv.2012.08.004

[56] Y. Zou, L. Bo, Z. Li, "Recent progress in human body energy harvesting for smart bioelectronic system", *Fundam. Res.*, **1**(3), 364, (2021). http://doi.org/10.1016/j.fmre.2021.05.002

[57] J. Wang, S. Li, F. Yi, Y. Zi, J. Lin, X. Wang, Y. Xu, Z. L. Wang, "Sustainably powering wearable electronics solely by biomechanical energy", *Nat. Commun.*, **7**(1), 12744, (2016). http://doi.org/10.1038/ncomms12744

[58] T. Yildirim, M. H. Ghayesh, W. Li, G. Alici, "A review on performance enhancement techniques for ambient vibration energy harvesters", *Renew. Sust. Energ. Rev.*, **71** 435, (2017). http://doi.org/10.1016/j.rser.2016.12.073

[59] B. Maamer, A. Boughamoura, A. M. R. Fath El-Bab, L. A. Francis, F. Tounsi, "A review on design improvements and techniques for mechanical energy harvesting using piezoelectric and electromagnetic schemes", *Energy Convers. Manag.*, **199** 111973, (2019). http://doi.org/10.1016/j.enconman.2019.111973

[60] B. Zhang, J. Chen, L. Jin, W. Deng, L. Zhang, H. Zhang, M. Zhu, W. Yang, Z. L. Wang, "Rotating-Disk-Based Hybridized Electromagnetic–Triboelectric Nanogenerator for Sustainably Powering Wireless Traffic Volume Sensors", *ACS nano*, **10**(6), 6241, (2016). http://doi.org/10.1021/acsnano.6b02384

[61] J. V. Vidal, V. Slabov, A. L. Kholkin, M. P. S. d. Santos, "Hybrid triboelectric-electromagnetic nanogenerators (E-TENGs) for mechanical energy harvesting: a review", *Nano-Micro Lett.*, (2021). http://doi.org/10.1007/s40820-021-00713-4